THE NEW HORIZONS RADIO SCIENCE EXPERIMENT (REX) [Submitted Draft 8jan07]

[Eq. (11) modified by A.C.Raugh, 29 Aug 2024 to correct errors noted post-publication]

G.L. TYLER[1], I.R. LINSCOTT[1], M.K. BIRD[2], D.P. HINSON[1], D.F. STROBEL[3], M. PÄTZOLD[4], M.E. SUMMERS[5], K. SIVARAMAKRISHNAN[1]

[1] *Packard 331, Dept. of Electrical Engineering, 350 Serra Mall, Stanford, CA 94305-4020, U.S.A.* (len.tyler@stanford.edu)

[2] *AIfA-Abteilung Radioastronomie, Universität Bonn, Auf dem Hügel 71, 53121, Bonn, Germany*

[3] *I121 Olin Hall, 34th and North Charles Streets, Johns Hopkins University, Baltimore, Maryland 21218, U.S.A.*

[4] *Institut für Geophysik und Meteorologie, Universität zu Köln, Albertus-Magnus-Platz, 50923 Köln, Germany*

[5] *Dept. of Physics and Astronomy, George Mason University, 4400 University Drive, MS-3F3, Fairfax, Virginia 22030-4444, U.S.A*

Received ; accepted

Abstract. The New Horizons (NH) Radio Science Experiment, REX, is designed to determine conditions on Pluto as manifest in the atmospheric state at the surface and a few scale heights higher. Expected absolute accuracies in n, p, and T at the surface are $4{\cdot}10^{19}$ m^{-3}, 0.1 Pa, and 3 K, respectively, obtained by radio occultation of a 4.2 cm-λ signal transmitted from Earth at 10–30 kW and received at the NH spacecraft. The threshold for

ionospheric observations is roughly $2 \cdot 10^9$ m^{-3}. Radio occultation experiments are planned for both Pluto and Charon, but the level of accuracy is expected to be useful for the neutral gas only at Pluto. REX will also measure the nightside 4.2 cm-λ thermal emission from Pluto and Charon during the time NH is occulted. At Pluto, the thermal scan provides about five half-beams across the disk; at Charon, only disk integrated values can be obtained. A combination of two-way tracking and occultation signals will determine the Pluto system mass to about 0.01 percent, and improve the Pluto-Charon mass ratio. REX flight equipment augments the NH radio transceiver used for spacecraft communications and tracking. Implementation of REX required realization of a new CIC-SCIC signal processing algorithm; the REX hardware implementation consumes 0.33 W, and has mass of 3.5 g in 1.25 cm^3. Commissioning tests conducted after NH launch demonstrate that the REX system is operating as expected.

Keywords: Pluto, Charon, radio science, radio occultation, Pluto atmosphere, Pluto thermal emission, New Horizons

1. Introduction

1.1. Overview

The New Horizons (NH) Radio Science Investigation, or Radio Experiment, 'REX,' addresses several specific questions related to the Pluto-Charon system. Primary among these is determination of surface conditions on Pluto

manifest in atmospheric temperature and pressure, with the expectation that the structure of the neutral atmosphere in the first few scale heights will be determined to useful accuracies. Secondary objectives include a search for and, if possible, measurement of the ionosphere of Pluto and measurement of the 4 cm-λ thermal emission temperatures on the nightsides of Pluto and Charon. Tertiary objectives include determination of the occultation chords of Pluto and Charon to very high accuracy as a constraint on the sizes, and an independent determination of the Pluto-Charon system mass and possible separation of the individual masses of Pluto and Charon. These goals are summarized in Table I.

The Pluto Science Definition Team (SDT) also identified the neutral atmosphere of Charon as a goal for a first mission. This is omitted from the current list as the presence of such an atmosphere appears to be ruled out at the level of REX sensitivity by ground-based stellar occultation measurements (Person et al., 2006). Similarly, the SDT objective of observations of solar wind effects on the ionospheres of Pluto and Charon can be inferred if sensible ionospheres are extant at the time of the NH flyby (Person et al., 2006).

Planned REX observations are based on the study of radio propagation effects along the path connecting NH with the Earth, and on inferred motions of NH with respect to Earth. The experiment employs occultation geometry

Table I. Objectives of NH REX Investigations.

Atmosphere (I)	$n(h)$, $T[p(h)]$	Pluto
Ionospheres (II)	$n_{e^-}(h)$	Pluto & Charon
Surface Emission Temperature (II)	T_{sur}	Pluto & Charon
Occultation Chord (III)	L entry–exit	Pluto & Charon
Masses (III)	$GM_{\rm sys}$, $GM_{\rm P}$, $GM_{\rm C}$	System & P, C

for sensing of Pluto's atmosphere. This observation requires the use of a highly stable source to produce a signal of precisely known characteristics and a receiver of comparable stability to capture the refracted signal after it emerges from the atmosphere. The REX instrument must capture the physical properties of the emergent signal. For this purpose, NH makes use of a new radio system design, flown once previously on MESSENGER (Srinivasan et al., 2007), which implements an onboard receiving system that captures signals transmitted from the ground. The REX experiment is enabled by adding a small amount of signal processing hardware to the radio system planned for communication and tracking of the NH spacecraft. This differs most other U.S. missions conducting occultation experiments in which transmissions from the spacecraft are received on the ground. As explained below, this change is necessary to meet the NH objectives, owing primarily to the great distance from Earth to the Pluto system.

In order to understand the importance of this change it is necessary to relate the approach taken in the design of the NH system to earlier methods. Previous practice for U.S. planetary spacecraft has been to use radio transponders in which 'uplink' signals derived from ground-based H_2 masers are received, filtered, amplified, and then used to derive a coherently related downlink signal which is transmitted to a receiving Earth station (for Voyager and Cassini examples *v.* Tyler (1987) and Asmar et al. (2005)). Under normal operating conditions this method guarantees a known relationship between the frequencies and phases of the 'uplink' and 'downlink' signals received and transmitted by the spacecraft, respectively; the ratio between the uplink and downlink frequencies, and hence the phases, is by design always of the form M/N, where M and N are integers, and where the phase may be offset by an unknown but constant amount. This approach results in a round trip stability that approaches that of the master atomic clock used to derive the original uplink signal.

The use of coherent transponders is extremely effective for precision tracking of deep space vehicles, and was also used for the conduct of radio occultation experiments using the NASA Deep Space Network prior to Voyager (see below). For radio occultation this method works well in the case of 'thin' atmospheres, such as that of Mars, where it was first used, but is susceptible to loss of coherence as a result of rapid changes in signal frequency and strength (*i.e.*, scintillations) and the occurrence of multiple

atmospheric paths when applied to 'dense' atmospheres, such as that of Venus and the gas giants.

The problem of loss of coherence was addressed at the time of Voyager by the inclusion of a highly stable quartz oscillator frequency reference onboard the spacecraft for use as the downlink reference during occultation events. Such oscillators, referred to as 'USO's (for ultra-stable oscillators) achieve levels of coherence over time intervals of 1–100 s that approach that of H_2 masers. (USOs are 1 to 1-1/2 orders of magnitude less stable than masers on time intervals of roughly 1,000–10,000 s, however.) Onboard USO frequency references have also been used effectively on several other missions to the outer planets, Mars, and Venus. Over time, USOs have proven to be extremely effective in a number of other areas related to mission operations design, as well as for science. In the Voyager-style implementation, though, the USO is considered to be an auxiliary device external to the standard transponder.

The REX investigation team will also NH cruise and far encounter data for studies of the solar wind, the solar corona, and for investigation of the 'Pioneer Anomaly' (Anderson et al., 1998, 2002) to the extent that this can be supported by the in-flight performance of the radio tracking system. These possibilities are not discussed further here, however.

1.2. Implementation

The REX investigation is based on the use of radio signals traveling between large ground transmitters, operated by the NASA Deep Space Network at three locations around the world, and a receiving system onboard the New Horizons spacecraft. For the primary investigation of the atmosphere of Pluto and the ionospheres of Pluto and Charon, the method of sensing is the detection of small perturbations in these signals. The direction of transmission is exclusively from the ground to the spacecraft. Ancillary investigations of gravitational parameters make use of round-trip Earth-spacecraft-Earth measurements with the NH tracking system.

The use of an uplink signal for these investigation is driven, directly and indirectly, by the great distance to Pluto. First, large signal-to-noise ratios (SNRs) at Pluto are required to support accurate measurements of Pluto's tenuous atmosphere, leading directly to the use of large transmitter powers. Second, the large flyby velocities limit the total available observation time for occultation measurements of Pluto's atmosphere to minutes, and the observations of the lower atmosphere to several seconds, increasing the required SNR further.

While occultation measurements based on the use of spacecraft transmitters are routine for thick atmospheres from orbiting and flyby spacecraft at bodies closer to Earth, this is not possible for NH at Pluto. The use of

large Earth-based transmitters providing increases in transmitter power by 3–4 orders of magnitude over spacecraft systems, with signal reception at the spacecraft, makes radio occultation measurements of Pluto's atmosphere practical.

As REX requires the coordinated use of Earth-based transmitters and a NH spacecraft receiver, REX comprises two elements. The first is the "Ground Element" made up of the DSN hardware and operations facilities supporting the NH mission, and the second is the "Flight Element" consists of a small amount of specialized signal processing hardware onboard the NH spacecraft. As the DSN support capabilities for radio science activities are well documented (Asmar et al., 2005), we will not discuss the REX Ground Element further.

The New Horizons radio system incorporates a USO as an inherent component in its design. In the approach adopted by NH, the spacecraft transmitter is always referenced to an onboard USO which is entirely independent in its functioning from the received uplink signals. This is unusual in precision deep space Doppler tracking systems. Typically such systems make use of the uplink signal transmitted from the ground to establish the downlink signal frequency, so that there is a known relationship between the frequency of the uplink received onboard that the downlink radiated by the spacecraft, thereby making possible an accurate calculation of the spacecraft radial velocity from a comparison of the transmitted uplink and received

downlink frequencies. In the NH case, the necessary link between the uplink signals received by the spacecraft and the downlink signals received by the ground tracking station is established by an onboard measurement of the received uplink frequency relative to the spacecraft USO. This is accomplished by counting the difference between the number of radio frequency cycles arriving at the spacecraft on the uplink relative to the number of cycles of oscillation of the USO in the same period. The observed frequency difference is returned to the ground by telemetry. In this system of tracking it is necessary to solve for both USO frequency as well as the round trip Doppler shift. Observation on the ground of the received one-way signal derived from the USO plus the measurements of the frequency difference measured onboard—taking into account the inherent difference in frequency between the ground transmitter and the USO—is sufficient to solve for the two unknowns.

The advantages of this approach are i) simplification of the radio system design, ii) increased stability of the downlink in the absence of an uplink signal from the ground, and iii) increased operational flexibility in conducting scientific investigations based on use of the radio system. Because the downlink in this type of system is independent of the uplink, the NH radio system is referred to as a "transceiver" rather than a "transponder." This system is discussed further by Deboy et al. (2005), Fountain et al. (Sp. Sci. Revs. this issue), Jensen & Bokulic (2000), and others.

Figure 1 illustrates the receiver portion of the NH transceiver and the integration of the REX hardware within the receiver. The amplifier chain is a conventional heterodyne design. The noise performance of the receiver has been improved over previous implementations by locating the leading low-noise amplifier (LNA) close to the antenna to reduce the physical temperature of the wave guide connecting the LNA to the high-gain antenna (HGA). The various mixing frequencies, $f_{\rm LO}$, for the intermediate frequency (IF) amplifier stages are derived from the USO, as are the clock reference frequencies used to drive the analog-to-digital converter. The REX portion of the system, which follows the 4.5 MHz buffer and anti-aliasing filter, is made up of an analog-to-digital converter (ADC) which feeds a triply-redundant programmed gate array (FPGA). This gate array implements the two data processing functions required by the REX experiment. These are i) calculation of the total power in the 4.5 MHz bandwidth containing the uplink signal that enters the antenna, and ii) processing of the 4.5 MHz data stream to isolate the ≈ 1 kHz portion of the frequency spectrum containing the occultation signals in order that these can be returned to the ground efficiently. The output of both processes is passed to the NH onboard data memory for later transmission to Earth.

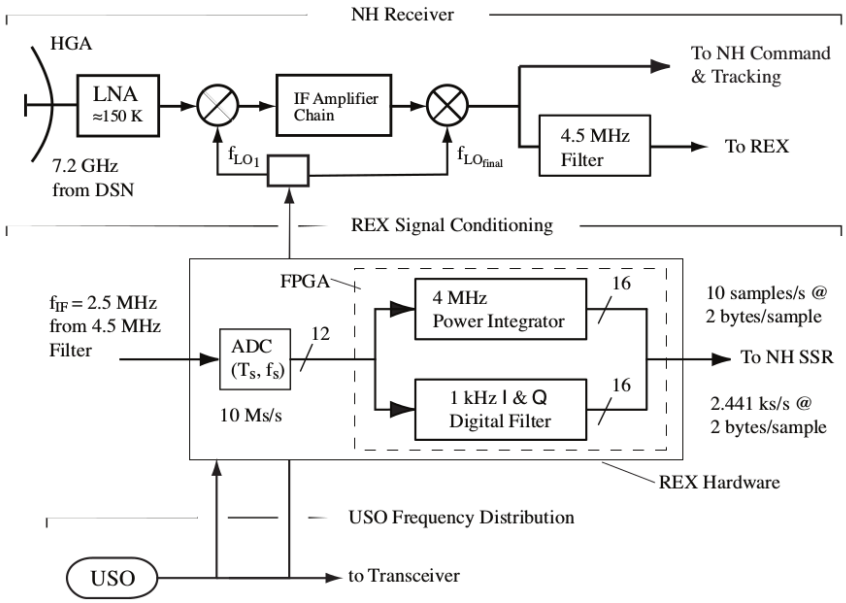

Figure 1. Overview of REX Onboard Implementation. Top section of figure shows functions of receiver portion of the NH transceiver. Following the 'IF Amplifier Chain,' the lower signal path with 4.5 MHZ Filter drives the input to the REX hardware imbedded in the transceiver; the upper path drives the uplink data processing functions of the transceiver. REX signal conditioning hardware, located with the labeled rectangle, functionally comprises ADC and a gate array programmed as a digital down-converter to 0 Hz, followed by a filtering and decimation step to reduce data volume, see Sections 1.2, 5.3, and Appendix. The output data are transmitted to the spacecraft memory for storage and later return to Earth by telemetry. The transmitter side of the transceiver shares the HGA. USO, bottom, serves as frequency reference for essential functions in transceiver and REX.

Table II provides the basic physical and power attributes of REX. The values in the table refer to the ADC and FPGA shown in Fig. 1 plus the electronic structure supporting these elements.

Table II. REX Onboard Resource Usage. REX in addition to the ADC and FPGA shown in Fig. 1, REX receives stable clock signals from USO used for navigation and amplified input signals from the NH transceiver.

Mass (g)	Power (W)	Volume (cm^3)
160	1.6	520

Tables III and IV together summarize the system aspects of REX.. In Table III note that the ground transmitter power and antenna gain are minimum values. Table IV lists the expected signal-to-noise ratios (SNR) for four combinations of transmitter power and antenna size in routine use at DSN ground stations. As the DSN is currently studying options for future configurations of ground stations, the levels of transmitter support available during the Pluto system encounter in 2015 are not known with certainty, but are expected to be within the range reflected by the options in Table IV.

Table V summarizes the radiometric performance expected of the REX instrument. Values in the table represent the limiting statistical uncertainties in measurement of frequency (f) and power (P) in coherent signals received

Table III. Summary of REX Link Parameters. λ = Operating wavelength, $P_{\rm rad}$ = Power radiated by DSN ground station, $G_{\rm gnd}$ = 34 m dia. ground station antenna gain, $G_{\rm s/c}$ = NH 2.1 m spacecraft antenna gain, $T_{\rm sys}$ = NH Transceiver system temperature.

λ	$P_{\rm rad}$	$G_{\rm gnd}$	$G_{\rm s/c}$	$T_{\rm sys}$
4.18 cm	10 kW (min)	$\approx$ 66 dBi (min)	$\approx$ 42 dBi	$\approx$ 150 K

by REX ($\delta f/f$ and $\delta P/P$) and the statistical uncertainty in the measurement of emission temperature in the absence of a coherent signal (δT). The variation in power represented by $\Delta P/P$ is that resulting primarily from uncertainties in spacecraft antenna pointing. Although pointing errors vary over periods of tens of seconds or longer they are highly correlated on much shorter periods of time, in contrast with noise-driven uncertainties that essentially change with each data sample. For occultation observations over intervals of 1 s the system SNR is the limiting error in determination of received power, while $\delta f/f$ is determinant for retrieval of the atmospheric structure. For other REX observations in the Pluto system $\delta f/f$ and $\delta T/T$ represent the primary experimental limitations.

Table IV. NH/REX Expected SNR. Signal to noise ratio achieved will depend on ground configuration extant at the time of Pluto system encounter. Capabilities depend on the combination of transmitter power and antenna available, or their equivalent. The 10 kw, 34 m. dia. combination satisfies basic REX requirements.

Uplink Power	Ground Antenna Dia.	
(kW)	34 m.	70 m
10	49.8 dB	55.8 dB
20	52.8	58.8

1.3. Pluto Encounter

The REX encounter with the Pluto system is focused on occultations by Pluto and Charon with the goals listed above. These occultations provide opportunities for characterization of Pluto's atmosphere and possibly a sensible ionosphere, and to search for a sensible atmosphere and ionosphere of Charon. The time difference between the entry and exit events will provide the length of the occultation chords. Occultation events also provide opportunities to observe thermal emission from Pluto and Charon. By maintaining

Table V. NH/REX Radiometric Performance. $\Delta f/f$ = Expected limiting uncertainty in uplink frequency measurement, $\delta P/P$ = Statistical error due to noise, $\Delta P/P$ = Typical error from HGA pointing, δT = Expected 1-σ uncertainty in thermal emission temperature, for conditions at Pluto.

$\delta f/f$	$\delta P/P$	$\Delta P/P$	δT
$\approx 5 \cdot 10^{-13}$	$\sqrt{\text{SNR/s}}$	≈ 0.05 dB	≈ 0.1K

the pointing direction of the HGA in the Earth direction while NH is behind each body, the motion of the spacecraft causes the antenna beam to sweep across the nightside of Pluto and Charon. At Pluto this strategy will yield approximately five half-beam resolution elements arranged diametrically in a line across the disk. At Charon, however, the distance behind the body is such that the antenna beam is larger than the obscured disk. Results for gravity will be derived from tracking data during approach to and recession from the system, and from occasional opportunities around the times of occultation observations. In this instance, baseline occultation data analyzed to obtain the uplink Doppler shift referenced to the onboard USO, though of lesser quality than two-way Doppler observations, may prove useful in

this regard. Details of these measurements are discussed individually in subsequent sections of this paper.

1.4. Encounter Geometry

Figure 2 shows he New Horizons encounter geometry. Not shown are the relative positions of Earth and Sun. Some details of timing and other conditions at closest approach can be found in Table VI. In the figure the path of NH through the system passes between the orbits of Pluto and Charon, but at a time when Charon is located opposite Pluto from the spacecraft. After closest approach to Pluto, the spacecraft proceeds to fly behind Pluto's disk at a distance of about 37 $R_{\rm P}$, and then behind Charon at a much great distance amounting to roughly 177 $R_{\rm C}$. The occultation at Pluto is targeted to be diametric with respect to the Earth for the radio event, which also works well for the UV solar occultation experiment owing to the closeness of NH behind Pluto and the closeness of Earth and Sun in the sky. At Charon the UV observations are optimized by making this event close to diametric with respect to the sun. As a result the radio occultation chord is expected to lie a large fraction of the Charon's radius from the center of the disk, depending on trajectory delivery errors.

Not shown in Fig. 2 are the relative positions of Earth and Sun. These have been optimized for the radio and UV occultation events by the choice

Table VI. Pluto System Encounter Geometry. Nominal geometric parameters for NH closest approach (C/A) to Pluto and Charon, July 14, 2015. Included angle is that between the direction of motion of the spacecraft and the LOS direction from spacecraft to Earth. See Tables IX and X for details.

NH spacecraft	Distance to Earth	31.90 AU
	Included angle, NH velociy and LOS	171.4°
	Flyby velocity	13,785 km/s
Pluto C/A	Time	11:59:00 UTC
	Distance	11,094 km
Charon C/A	Time	12:12:51 UTC
	Distance	26,925 km

of the NH trajectory and arrival date in the Pluto system. In this regard, two factors played into the trajectory selection. First, in planetary occultations there is often a conflict between UV solar and radio experiments owing to the differing directions from the spacecraft to the sun and to Earth, respectively. Second, the anticipated radio occultation effects, expressed as an apparent change in radio path length, will be a small fraction of the radio wave length.

A radio signal traveling between Earth and Pluto typically encounters significant phase fluctuations in passing along the path through the solar

wind, and such can be expected in general for the $\approx$ 40 AU path between Earth and Pluto. Solar wind fluctuations arise primarily from the advection of irregularities in solar wind density across the propagation path, thereby introducing a time-variation on scales of seconds to hours in the radio (optical) path length. Radio ray paths that are aligned radially away from the Sun are relatively immune to this effect, however. Nevertheless, changes in path structure can occur to varying degree along the radial direction on time scales of hours, primarily by the introduction of new solar wind material at the path end nearest the sun.

NH mission planning has addressed the issues of *i*) solar UV and radio occultation and *ii*) solar wind induced noise by choosing solar opposition for Pluto system encounter. For the opposition geometry, the angular separation of Sun and Earth as viewed from NH is only 0.23°, while the radio propagation path is at a minimum of 4.2° from a solar radial at the Earth end, and. This choice optimizes the potentially conflicting requirements for the UV-solar and radio-Earth occultation observations while reducing solar wind scintillation to the minimum possible.

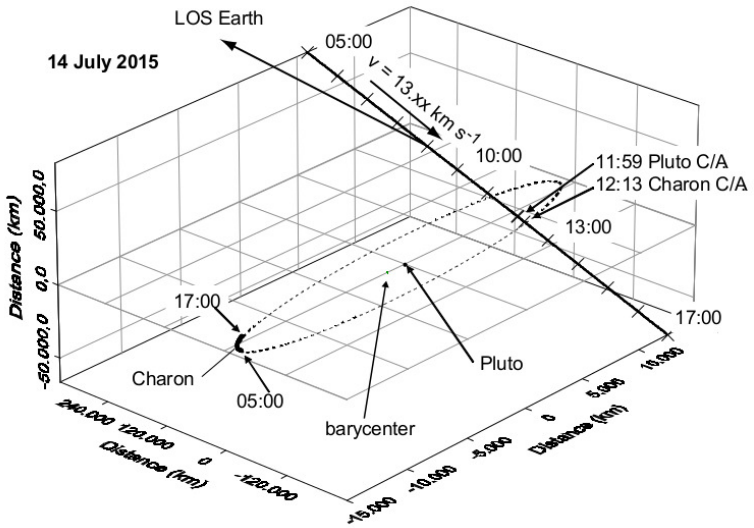

Figure 2. Geometry of NH encounter with the Pluto-Charon system. NH flight through the Pluto-Charon system visually follows a straight line $\approx 7.1^\circ$ from the line-of-sight to Earth, with a bending angle of only $\approx 0.00...^\circ$ [[TBS]]. During the interval of closest approach to Charon is located approximately opposite Pluto from NH.

2. Radio occultation sounding of Pluto's atmosphere

2.1. Introduction

The reconnaissance of the Neptune system by Voyager 2 included a radio occultation experiment that successfully sounded the tenuous neutral atmosphere of Triton (Tyler et al., 1989). This experiment was conducted in the conventional downlink configuration, using radio signals transmitted by Voyager 2 and received by terrestrial tracking stations equipped with large-diameter antennas. The data at 3.6 cm wavelength had a fractional frequency

stability δ/f of $\sigma_{\mathrm{Allan}} \approx 2 \cdot 10^{-12}$, where σ_{Allan} is the Allan deviation set by the ultra-stable oscillator (USO) onboard Voyager 2, and a concomitant signal-to-noise ratio (SNR) of 45 dB in a 1-Hz bandwidth. Analysis of these data initially yielded a surface pressure of 1.6 ± 0.3 Pa ($16 \pm 3\mu$bar), later refined to 1.4 ± 0.1 Pa (Gurrola, 1996), and a constraint on the average scale height of the lower atmosphere, but the observational data were too noisy to permit reliable atmospheric profiles to be obtained through data inversion.

Pluto's atmosphere is believed to be similar to Triton's in that both atmospheres are comprised predominantly of N_2, plus trace gases such as CO and CH_4 in uncertain abundances, and with surface pressure determined by vapor-pressure equilibrium. In designing a radio occultation experiment to sound Pluto's atmosphere we therefore drew heavily on lessons learned with Voyager 2 at Triton. The New Horizons radio system includes two key enhancements relative to Voyager 2. First, New Horizons carries two USOs, each with a fractional frequency stability of $\sigma_{\mathrm{Allan}} \approx 2 \cdot 10^{-13}$. Second, the New Horizons experiment will be conducted in an uplink configuration that exploits the high-power transmitters available at tracking stations of the NASA Deep Space Network (DSN), thereby making it possible to obtain precision measurements in the short period of time available during the Pluto occultation. The resulting SNR of the data recorded onboard New Horizons will be about 55 dB in a 1-Hz bandwidth, commensurate with the enhanced frequency stability of the onboard USOs. For New Horizons

the two critical parameters of frequency stability and SNR are improved by about an order-of-magnitude with respect to their counterparts on Voyager 2 at Titan.

2.2. Background and motivation

Before further discussion of the radio occultation experiment, we review briefly the fragmentary understanding of Pluto's atmosphere that has emerged from Earth-based observations during the past few decades. Our goals here are to provide a context for describing the capabilities of REX and to identify major questions that the instrument is uniquely qualified to address.

Observations of sunlight reflected by Pluto in the near-infrared spectral region provide strong constraints on the identity and relative abundances of surface ices. High-albedo surface units are dominated by solid N_2, with frozen CH_4 and CO as trace constituents (Owen et al., 1993; Cruikshank et al., 1997; Grundy and Buie, 2001). Among the ices identified on the surface, N_2 is not only the most abundant but also the most volatile (Brown and Ziegler, 1979], so that it is widely believed to be the dominant component of the atmosphere (e.g., Cruikshank et al., 1997; Yelle and Elliot, 1997). The atmosphere should contain traces of both CH_4 and CO, but their mixing ratios are unknown.

Photometric observations of Pluto's occultation of the star P8 in 1988 provided decisive evidence for the presence of an atmosphere and important constraints on its thermal structure (Hubbard et al., 1988; Elliot and Young, 1992). Yelle and Elliot (1997) reviewed the implications of these measurements. In high-quality data recorded by the Kuiper Airborne Observatory (KAO), the slope of the light curve changes abruptly near the half-light level at both ingress and egress, marking a significant transition in atmospheric structure at a radius of about 1215 km. Above this level the atmosphere is nearly isothermal with a pressure scale height of approximately 56 km, corresponding to a temperature of about 104 K for a pure N_2 atmosphere (Elliot and Young, 1992; Millis et al., 1993). The stellar occultation results are ambiguous with respect to structure of the lower atmosphere, as the distinctive slope change in the light curve could arise either through extinction by atmospheric aerosols (Elliot et al., 1992; Elliot and Young, 1992; Millis et al., 1993) or from the refractive effects of a strong temperature inversion (Eshleman, 1989; Hubbard et al., 1990). By enhancing the refractive bending of starlight, such an inversion could also conceal the presence of an underlying troposphere (Stansberry et al., 1994).

Neither Pluto's radius nor the pressure at the surface can be determined with confidence from observations of the 1988 stellar occultation (Stansberry et al., 1994; Yelle and Elliot, 1997). The data preclude a radius larger than about 1200 km and a surface pressure less than roughly 0.3 Pa, but

the measurements cannot discriminate among diverse models for the lower atmosphere, including one with a 40-km deep troposphere, a radius of 1160 km, and a surface pressure of about 2.4 Pa (Stansberry et al., 1994).

An occultation of the star P131.1 by Pluto, as viewed by an array of ground-based telescopes in 2002, revealed a significant increase in the total mass of Pluto's atmosphere (Elliot et al., 2003; Sicardy et al., 2003). In the region above roughly 1215 km radius, the atmosphere remains isothermal and the temperature appears essentially unchanged since 1988, but the pressure at a fixed radius of 1215 km has doubled, increasing from about 0.23 Pa in 1988 to about 0.50 Pa in 2002. It is expected that the surface pressure has probably increased by a similar factor, although the structure of the lower atmosphere and the surface pressure remain highly uncertain.

Hansen and Paige (1996) predicted such an increase in surface pressure, and modeled the seasonal evolution of an N_2 atmosphere in vapor pressure equilibrium with surface frost. In this model, sublimation and condensation of N_2 are controlled by the heat balance of surface frost and, consequently, vary with latitude and season. The net result is a surface pressure that depends not only on the distance of Pluto from the sun but also on the subsolar latitude. The vapor-pressure equilibrium model predicts that the peak surface pressure on Pluto would occur not at perihelion in 1989 but would be delayed by 2–3 decades to the time when the subsolar latitude moves from the equator into the northern hemisphere, exposing a polar

cap of solid N_2 to increasing solar heating. In this senario, a precipitous decrease in surface pressure is expected to begin in roughly the period around 2025 as the north polar N_2 cap is depleted, the south polar cap grows, and Pluto continues to recede from perihelion (Fig. 11, Hansen and Paige, 1996,). The accuracy of this model is limited by large uncertainties in the albedo and emissivity of the frost, the albedo and thermal inertia of the substrate, the total nitrogen inventory, and the behavior of multicomponent ices, particularly N_2 contaminated with traces of CH_4 (Hansen and Paige, 1996; Spencer et al., 1997).

No observations of Pluto's extended upper atmosphere are currently available, but the atmospheric chemistry and the characteristics of the ionosphere have been explored with photochemical models (Summers et al., 1997; Krasnopolsky and Cruikshank, 1999). In the ionosphere, the models predict a strong dependence of both ion composition and peak electron density on the currently unknown abundances of CO and CH_4. The vertical distribution of CH_4 depends in turn on its abundance near the surface and the rate of vertical transport. If the Pluto CH_4 mixing ratio near the surface is relatively small, as on Triton, it is expected that CH_4 would be destroyed photochemically in the lower atmosphere, leaving the ionosphere dominated by relatively long-lived atomic ions such as N^+ and C^+. In this instance the peak electron density can be as large as about 2,000 cm^{-3} (Summers et al., 1997, Figure 8). If, on the other hand, the CH_4 mixing ratio near the surface

is sufficiently large, then the resulting enhancement in CH_4 abundance at high altitudes would ensure that the ionosphere is dominated by molecular ions. Consequently, the relatively fast recombination then limits the peak electron density to roughly 800 cm^{-3} (Summers et al., 1997, Figure 10; Krasnopolsky and Cruikshank, 1999).

Pluto's size has been the subject of numerous investigations using several diverse techniques (Tholen and Buie, 1997). The best results to date have been obtained from mutual event photometry (e.g., Young and Binzel, 1994) and direct imaging with the Hubble Space Telescope (Albrecht et al., 1994). (v., ????, below) According to these observations, Pluto's radius lies between about 1150 and 1180 km, with a typical uncertainty of 15 km (Tholen and Buie, 1997, Table III). Pluto's volume is therefore known to an accuracy of approximately 4 percent.

Pluto's mass has been determined from HST images of Pluto and its three known satellites (Buie et al., 2006). The combined mass of Pluto and Charon is $(1.4570 \pm 0.0009) \cdot 10^{22}$ kg, while the Charon-to-Pluto mass ratio is 0.1165 ± 0.0055, yielding a mass for Pluto of $(1.3050 \pm 0.0064) \cdot 10^{22}$ kg. As the mass uncertainty is only about 0.5 percent, the radius is the limiting factor in current estimates of Pluto's density.

2.3. Experiment objectives, methods of analysis, and predicted performance

2.3.1. *Pluto's radius.*

The New Horizons radio occultation experiment will determine Pluto's radius to an uncertainty of much less than 1 km. The occultation is nearly diametric by design, minimizing the sensitivity of this measurement to errors in the spacecraft trajectory. In addition, because extinction by aerosols is negligible at centimeter wavelengths the radio occultation radius is insensitive to the presence of an optically thick limb haze, e.g., as in the radio occultation of Voyager 1 by Titan (Lindal et al., 1983). When this new radius measurement is combined with previous determinations of Pluto's mass, the mean density of Pluto will be known to less than 1 percent, comparable to the current uncertainty for Triton (Tyler et al., 1989; McKinnon et al., 1995).

The data recorded by REX during the Pluto occultation will contain not only the effects of Pluto's atmosphere, as discussed below, but also an extended diffraction pattern caused by the surface. We will remove these diffraction effects from the data through use of an established technique, alternately called inverse Fresnel filtering or back propagation. First developed and applied in connection with radio occultation studies of planetary rings (e.g., Marouf et al., 1986; Tyler, 1987; Gresh et al., 1989) and later

adapted for use in atmospheric occultations (e.g., Tyler et al., 1989; Karayel and Hinson, 1997; Hinson et al., 1997, 1998), this technique for excising limb effects is well understood. When applied to Pluto, this method of analysis will allow atmospheric sounding without interference from diffraction effects while yielding an accurate solution for Pluto's radius.

As an example of this technique, Fig. 3 shows results obtained by applying inverse Fresnel filtering to radio occultation measurements obtained with Mars Global Surveyor. This experiment sounded the atmosphere of Mars at 293.3E, 67.2N on 31 December 1998; the data quality is comparable to what will be obtained with New Horizons at Pluto (e.g., Hinson et al., 2001). The unfiltered intensity data (Fig. 3a) are strongly modulated by diffraction from the surface of Mars. Information about the location of the surface is distributed across a pattern of more than 40 diffraction fringes extending to more than 5 km in radius behind the geometric limb of Mars. Inverse Fresnel filtering of these data removes not only the surface diffraction pattern but also the effects due to refractive bending in the atmosphere, as shown in Fig. 3b. The filtered data resemble a step function, with the signal intensity dropping by nearly 30 dB, or a ratio of 1,000:1, in a radial span of 30 m, yielding a clearly defined local radius of 3,375,742 $\pm$ 10 m. This result is consistent with independent measurements of the surface radius at this location by the Mars Orbiter Laser Altimeter (Smith et al., 2001). The uncertainty in radius, about 10 m, is smaller by a factor of 50 than the

characteristic Fresnel scale of the diffraction pattern, which is 490 m for the geometry and wavelength of this MGS experiment. The Fresnel scale for New Horizons will be about 1,350 m, suggesting that Pluto's radius at the occultation point can be determined with a precision of about 30 m.

2.3.2. *Pluto's neutral atmosphere.*

The New Horizons radio occultation experiment will sound the near-surface neutral atmosphere of Pluto at both ingress and egress. The sensitivity of these measurements is sufficient to allow retrieval of accurate vertical profiles of number density (n), pressure (p), and temperature (T) that extend from the surface to about the 0.2 Pa pressure level. Key results will include the first unambiguous measurements of atmospheric structure below approximately 1,215 km radius, as well as the values of n, p, and T at the surface. The experiment will reveal the detailed structure of any low altitude temperature inversion and will determine whether or not a deep troposphere is present and, if so, its characteristics.

In analyzing occultation data we will remove diffraction effects from the occultation data recorded by REX through inverse Fresnel filtering, as described above. Atmospheric profiles can then be obtained via the conventional Abel-transform retrieval algorithm (e.g., Fjeldbo et al., 1971; Tyler, 1987; Karayel and Hinson, 1997; Hinson et al., 1999), which has been applied

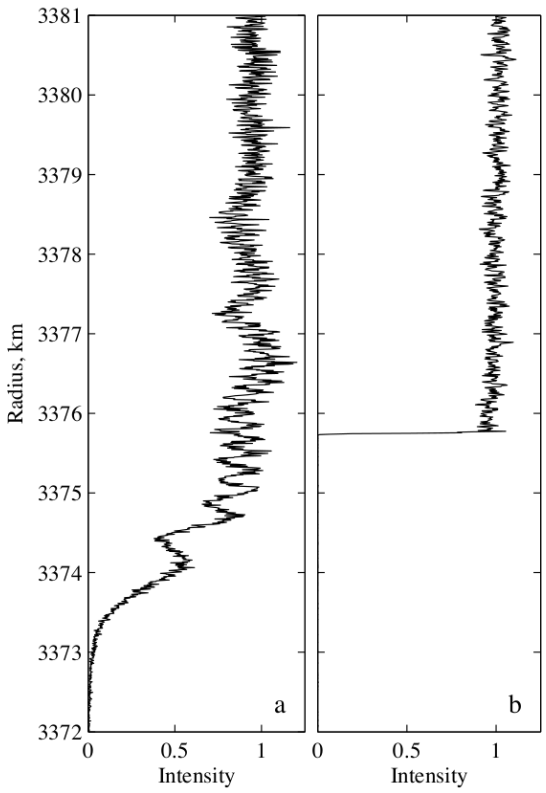

Figure 3. Measurements of signal intensity during a radio occultation experiment conducted with Mars Global Surveyor on 31 December 1998. (a) Original data with a sample spacing of approximately 5 m. The diffraction pattern produced by the surface of Mars contains > 40 diffraction fringes and extends more than 5 km beyond the limb of Mars. Refractive bending in the lower atmosphere deflects the diffraction pattern into the geometric shadow of Mars by ≈ 2 km. (b) Intensity measurements after inverse Fresnel filtering. Abrupt drop in intensity marks the location of the surface.

extensively in occultation experiments throughout the solar system. By this procedure we will obtain vertical profiles of n, p, and T at both ingress

and egress. The profiles will be registered accurately in both planetocentric radius and altitude above the surface.

We conducted numerical simulations to characterize the expected performance of the radio occultation experiment at Pluto. For these calculations we adopted an uplink SNR of 55 dB in a 1-Hz bandwidth and a USO stability $\sigma_{\mathrm{Allan}} = 2 \cdot 10^{-13}$, consistent with prelaunch laboratory measurements. As discussed here, the NH trajectory will produce a diametric occultation. The plane-of-sky velocity of the spacecraft relative to Pluto will be 3.52 km/s, with a planned spacecraft-to-Pluto distance of 43,400 km at the midpoint of the occultation.

The atmospheric model used in the simulations is based loosely on the predictions of pure N_2, radiative-conductive models for Pluto's atmosphere (Strobel et al., 1996). The model pressure and temperature at the surface are 1.0 Pa (10 μbar) and 37 K, respectively, consistent with vapor pressure equilibrium (β-N_2). We based the model surface conditions on the results of the 2002 stellar occultation extrapolated downward to a conservative, i.e., relatively large, estimate of the surface radius of 1190 km. The model includes a strong temperature inversion in the lowest scale height above the surface, with the temperature increasing to 100 K at 0.5 Pa; at higher altitudes the profile is nearly isothermal. Figure 4 shows the vertical structure of the model in the lowest 50 km above the surface.

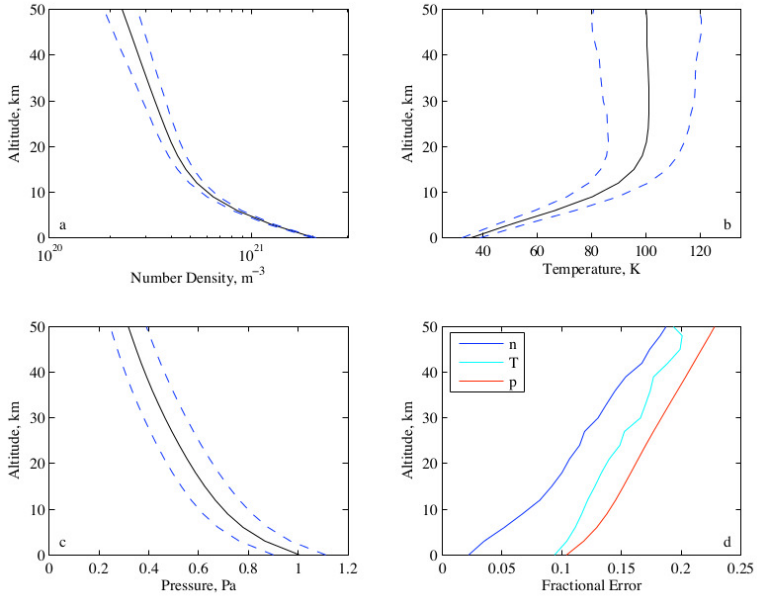

Figure 4. Simulated performance of radio occultation sounding of Plutos atmosphere with REX. Solid lines in the first three panels show profiles of (a) number density, (b) temperature, and (c) pressure of the model atmosphere used in the simulations; dashed lines in these three panels show 1-σ deviations of the radio occultation retrievals, as characterized by a 900-case Monte Carlo simulation. (d) Fractional errors in n, p, and T.

We used geometrical optics to calculate the signal variations that would be observed by REX during a radio occultation of this model atmosphere. A radio signal that grazes the surface of Pluto as it traverses this atmosphere will experience a phase shift of roughly 1 radian, about half as large as the effect produced by the atmosphere of Triton (Tyler et al., 1989); the equivalent increase in optical path length is about 6.6 mm. The peak angular deflection caused by refractive bending is 0.8 microradians, and the corre-

sponding Doppler shift observed by REX is roughly 70 mHz, which exceeds the frequency-noise fluctuations associated with the USO by a factor of 50:1 in a one second observation time.

We used the Monte Carlo method to characterize the accuracy of the retrievals in this simulated experiment. For this we applied the Abel-transform retrieval algorithm to 900 sets of simulated observations, each constructed by adding computer-generated random noise to the results of the forward calculations. The noise is uncorrelated from one sample to the next with a standard deviation determined by the simulated experimental SNR and the USO stability. Figure 4, (a) through (c), show the standard deviations in the retrieved profiles of n, p, and T. The radio occultation retrievals are inherently most accurate near the surface, as shown in Figure 4d. At the surface, the uncertainties in n, p, and T are $4 \cdot 10^{19}$ m^{-3}, 3 K, and 0.1 Pa, respectively, corresponding to fractional uncertainties of about 2 percent in n and 10 percent in both p and T.

The uncertainty in surface pressure can be reduced in several ways, such as by averaging results from ingress and egress or by imposing additional physical constraints to reduce the number of degrees for freedom in the result. The Abel-transform retrieval algorithm derives a pressure profile from the number density profile by assuming hydrostatic balance. An alternate estimate of surface pressure can be obtained by assuming vapor pressure equilibrium. Use of the ideal gas law along with the vapor pressure formula

for N_2 then allows the surface pressure to be derived directly from the number density at the surface. Owing to the very strong dependence of vapor pressure on temperature, the uncertainty in surface pressure is then commensurate with the uncertainty in number density, reducing its value from 10 percent (0.1 Pa) to about 2 percent (0.02 Pa). The actual method(s) of analysis chosen will depend on the nature of the data obtained.

2.3.3. *Pluto's ionosphere.*

We will also examine the radio occultation measurements for evidence of an ionosphere. On the basis of predictions by photochemical models (Summers et al., 1997; Krasnopolsky and Cruikshank, 1999), we expect the effect of Pluto's ionosphere on the radio signal received by REX to be comparable to the noise threshold. Detection should be possible if the peak electron density exceeds about $2{\cdot}10^3$ cm^{-3}, at the high end of current predictions, particularly if the lower ionosphere contains a sharp vertical gradient of electron density (e.g., Figure 8c, Summers et al., 1997,). Such an ionospheric feature would produce an appreciable phase shift in a relatively short time interval. If an ionosphere is detected, we will determine or constrain basic characteristics such as the peak density, the height of the peak, and the topside scale height.

3. Gravity Investigations

3.1. APPROACH

Radio-Doppler tracking of spacecraft flying by a planetary body is a powerful and precise tool for the determination of the acceleration constant product, GM, and hence M. Given M, and the radii as determined by a combination of calibrated imaging and radio occultation, the bulk density is readily found. The importance of a flyby determination of GM in the Pluto-Charon system lies in the opportunity to obtain values that are essentially independent of astrometry, as illustrated by the Voyager fllyby determination of the GM for Neptune (Standish, 1993), which obviated the need for "Planet X" and the opportunity to separate the masses of Pluto and Charon.

Using conservative values from past missions (e.g., Voyager (Tyler, 1982); Mars Global Surveyor (Smith et al., 1997); Rosetta (Pätzold et al., 2001)), and extrapolating the near-Earth performance of New Horizons to Pluto, typical accuracies in Doppler determination of the spacecraft line-of-sight velocity of approximately 20 μm s^{-1} can be expected, and values as low as 10 μm s^{-1} might be achieved, subject to conditions at the DSN tracking stations and in Earth's ionosphere and the solar wind. This level of performance may lead to an achievable accuracy in GM of, e.g., $5.6{\cdot}10^{-5}$ for the adopted values

of Pluto's bulk parameters (cf. Table VII) if the accuracy is driven by the measurement of $(\Delta v)_\infty$ alone (Anderson et al., 1992).

Ground based observations can determine only the system mass and the mass ratio. Radiometric observations by the New Horizons spacecraft during the Pluto system encounter will provide an independent determination of system mass to a very high accuracy. To the extent that radiometric observations are available during the periods which include the approximate closest approaches to Pluto and Charon, it will be possible to determine the masses of Pluto and Charon independently at comparable or better accuracies than current Earth-based observations.

We consider the approach outlined in the remainder of this section to the estimation of the Pluto and Charon masses. For this purpose we made use of the currently planned flyby geometry, Table VI and Fig. 2, as well as the bulk parameters discussed below and listed in Table VII.

Recent derivation of the system mass including Pluto and its three moons (Buie et al., 2006) yielded,

$$GM_{\rm sys} = (972.20 \pm 0.60) \cdot 10^9 \quad {\rm m}^3{\rm s}^{-2} \tag{1}$$

and a mass ratio of

$$k = \frac{M_{\rm C}}{M_{\rm P}} = 0.1165 \pm 0.0055 \tag{2}$$

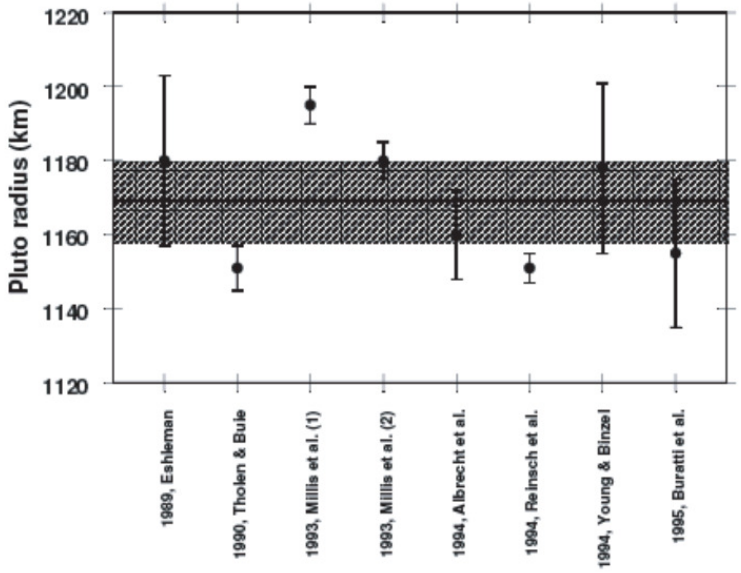

Figure 5. Observed radii of Pluto from mutual events. Note in particular that the value from 'Eshleman (1989)' is an upper bound derived from analysis of stellar occultation radii.

The actual mass estimates M_p and M_c for Pluto and Charon, respectively, are computed from a combination of the system mass, Eq. 1 and the mass ratio Eq. 2, and are shown in Table VII.

Figure 5 summarizes the various determinations of radii for Pluto together with their stated 1-σ uncertainties. Seven determinations of the radius of Pluto made after 1990 during the mutual events are roughly consistent with each other. All but one have uncertainties that either fall within or touch the range of their average behavior. The individual values, however, vary strongly and do not overlap within their error bars (Fig. 5). From Fig.

5 it is clear that the variation in recent determinations of Pluto's radius is in the range of 20 km. These determinations are subject to a systematic bias since the limb of Pluto appears be obscured by a persistent haze and there is no clear evidence that observed stellar occultation rays have reached the surface. Our adopted mean value and its one sigma error is listed in Table VII.

Until recently, the radius of Charon was even less well determined, although the absence of an obscuring atmosphere eliminates this as a source of bias. Person et al. (2006) determined the radius of Charon from stellar observations to a high degree of precision (see Table VII).

The densities shown in Table VII are those obtained using the estimates of the radi, the system mass, and the mass ratio just discussed.

The quoted uncertainties of the values in Table VII are a consequence of statistical uncertainties in the system mass, the mass ratio, and the radii. Bulk density values from the literature often assume a known fixed-body radius without error and result in bulk density values—particularly for Charon—that vary sufficiently as to lead to different models of the interior (cf. Gulbis et al., 2006; Buie et al., 2006). As noted above, the radius of Pluto is subject to the possibility of a systematic overestimation error as a result of atmospheric obscuration near the surface.

Table VII. Adopted Bulk Parameters for Pluto and Charon. Pluto radius is weighted mean of values in Fig. 5. Charon radius is from Person et al. $GM_{\rm P}$ and $GM_{\rm C}$ are from Eqs. 1 and 2. Masses of P and C are from the respective GMs plus value of G. Errors in radii, $GM_{\rm sys}$, k, and G have been propagated to tabulated values.

Pluto	Radius	1169 ± 12	km	1 %
	$GM_{\rm P}$	$8.708 \pm 0.043 \cdot 10^{11}$	$\mathrm{m^3\ s^{-2}}$	0.5
	Mass	$1.305 \pm 0.0065 \cdot 10^{22}$	kg	0.5
	Density	1950 ± 58	$\mathrm{kg\ m^{-3}}$	3.2
Charon	Radius	606 ± 1.5	km	0.2 %
	$GM_{\rm C}$	$1.014 \pm 0.04 \cdot 10^{11}$	$\mathrm{m^3\ s^{-2}}$	4
	Mass	$0.1520 \pm 0.007 \cdot 10^{22}$	kg	4.6
	Density	1631 ± 79	$\mathrm{kg\ m^{-3}}$	4.8

From Table VII, it is clear that the limiting factors in our knowledge of the densities of Pluto and Charon reversed for the two bodies. For Pluto, the 1 percent uncertainty in radius is limiting as it contributes 3 percent uncertainty to the density. For Charon it is the 4.6 percent uncertainty in mass which is limiting. The near-diametric radio occultation of Pluto will be definitive as to the radius even whether or not the limb is obscured optically.

By its flyby through the system, REX can also provide an independent means of separating the of masses, although the degree to which this can be accomplished is not well known at this point.

3.2. REX CONTRIBUTIONS

For the estimated values in Table VII we integrated the equation of motion for the planned 15 July 2015 New Horizon trajectory within the Pluto system based on an initial state (TBD-MP) hours prior to closest approach. We consider both the dominant gravitational forces and a model of the stochastic non-gravitational forces acting on the spacecraft. The primary observable is the line-of-sight (LOS) velocity, $v_{\rm LOS}$, between the spacecraft and the Earth-based receiving station, obtained by projecting the total velocity onto the direction to Earth. The angle between the direction to Earth and the direction of motion of the New Horizons spacecraft is approximately 171° (Fig. 2). As we are interested in the accelerations of the spacecraft as a result of the gravity of Pluto and Charon, we calculated the expected change in velocity component, $\Delta v_{\rm LOS}$, computed for the time interval within ±4 hrs of the closest approach to Pluto.

The Pluto and Charon curves in Fig. 6 are calculated for the trajectory with detailed parameters given in Tables IX and X. It should be clear

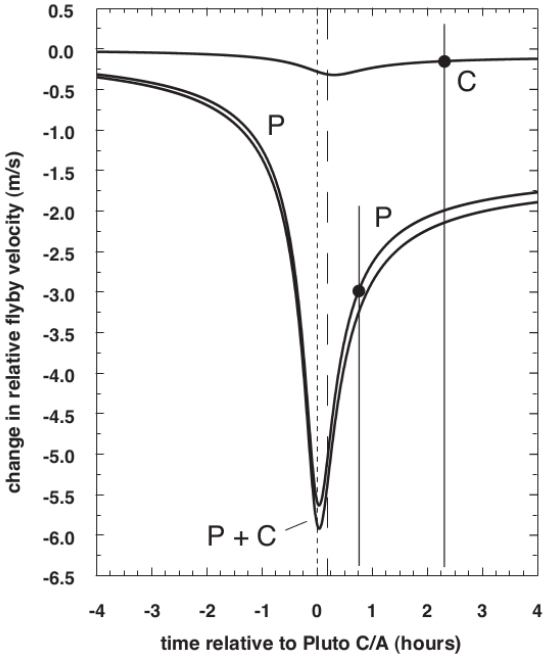

Figure 6. Line-of-sight velocities for Pluto and Charon. The three curves represent the individual contributions of Pluto (P) and Charon (C) to the total change in velocity, 'P + C.' The time scale is ±4 hrs from the time of closest approach of NH to Pluto. Stipled line is closest approach to Pluto; dashed line marks the closest approach to Charon, which occurs about 14 minutes later. Solid curves crossing marked points in P and C curves show values at times of occultation measurements.

that increasing/decreasing the masses of Pluto and Charon to first order increases/decreases the amplitude of the corresponding curve.

In Fig. 6, the units on the vertical scale, 0.5 m/s, represent 5,000 σ, even if the measurement error were to be as large 100 μm/s. The units on the horizontal scale, 1 hr, represent 60 samples of velocity obtained with a conservative one-minute integration time. These measurement accuracies,

together with the offsets between the points of maximum curvature, provide credible evidence that radiometric tracking data can be effective in determining the individual masses of Pluto and Charon.

Figure 6 illustrates the separate contributions of Pluto and Charon to the change in spacecraft velocity, again based on integration of the motion. Curve 'P+C' shows the variation in the total line-of-sight spacecraft velocity with the individual contributions from Pluto and Charon. The maximum change in velocity of the individual curves for Pluto and Charon occurs some minutes later than the times of closest approach to the two bodies. This is due to the projection of the Δv components across and along the trajectory into the LOS to Earth (the true observable). The curves would be symmetrical about their times of closest approach if the path of motion were parallel or anti-parallel to the line-of-sight.

After correcting the data for several other gravitational forces, e.g., third body and non-gravitational forces, e.g., solar radiation pressure, the values of GM for Pluto and Charon can be extracted from a series of observations during the fly-by interval by constraining the integration of the equation of motion to the actual observed points. The degree of accuracy to which this can be actually accomplished is not known as of this writing owing to uncertainties in the availability of tracking data during the encounter period. (Such availability is limited by the need to employ attitude maneuvers for instrument pointing, thereby taking the spacecraft high-gain antenna beam

off the Earth direction.) Two periods of certain Earth pointing occur during the radio occultations of Pluto and Charon.

It can be shown that for a flyby in which the change in $\sin\alpha$ is small, and where one observes the change in the line-of-sight velocity from well-before to well-after closest approach, or formally, for

$$(\Delta v)_\infty = \lim_{t=-\infty}(v) - \lim_{t=+\infty}(v) \tag{3}$$

that

$$(\Delta v)_\infty = -2\frac{GM_{\rm sys}}{v_0 d}\sin\alpha \tag{4}$$

where $(\Delta v)_\infty$ is the magnitude of the total change in the spacecraft velocity as a result of the close encounter with the Pluto system, v_0 is the relative flyby velocity at the point of closest approach, d is the distance of closest approach of the spacecraft to the barycenter, and α is the angle between the final direction of asymptotic motion and the LOS to Earth (Pätzold et al., 2001). As a practical matter, given the relatively small mass in the Pluto system and the high velocity of New Horizons approach to the Pluto system, $(\Delta v)_\infty$ can be based on observations within a few days before and after leaving the system.

The post-encounter change in velocity $(\Delta v)_\infty$ for Pluto and Charon together, *i.e.*, the change associated with the system, is approximately –1.8 $\mathrm{m\,s^{-1}}$, Fig. 6. Again, this is to be compared with the conservative estimate of expected thermal and system noise corresponding to LOS velocity errors

of the order of 20 μm s^{-1}. The post-encounter change in velocity $(\Delta v)_\infty$ for Pluto and Charon separately are estimated as 1.78 m/s and 0.086 m/s, respectively. (Also in Fig. 6.)

The utility of Eq. 4 is that it shows the direct connection between the change in velocity of a spacecraft test particle and the planetary mass. More precisely, the solution for the mass $M_{\rm sys}$ is proportional to $(\Delta v)_\infty$ since $(\Delta v)_\infty$ depend on M for a given flyby velocity and closest approach distance. Typical uncertainties in line-of-sight velocities from modern solutions for spacecraft trajectories are in the range of 20 μm s^{-1}, while distances of closest approach are usually accurate to within about 1 km; uncertainties in values for $\sin\alpha$ are negligible.

We may also use the analytic solution, Eq. 4, for a first-order error analysis. The relative error contributions to the determined GM value are,

$$\left(\frac{\sigma_{\rm GM}}{GM}\right)^2 = \left(\frac{\sigma_{\rm v_0}}{v_0}\right)^2 + \left(\frac{\sigma_d}{d}\right)^2 + \left(\frac{\sigma_{\Delta v}}{(\Delta v)_\infty}\right)^2 \tag{5}$$

where σ_{GM}, σ_{v_0}, σ_d, and $\sigma_{\Delta v}$ are the 1-σ errors contributing to the error in the value of GM. The relative flyby velocity v_0 and the closest approach distance d will be determined from orbit determination after the encounter and are expected to be accurate to much less than 0.0001 m/s and about 1 km, respectively. This implies that the fractional error associated with uncertainty in the velocity observations is,

$$\frac{\sigma_{\rm v_0}}{v_0} = \frac{10^{-3}}{13,785}\frac{\rm m\,s^{-1}}{\rm m\,s^{-1}} = 7.2\cdot 10^{-8} \tag{6}$$

which is a very small contribution to the total error.

The error contribution from the closest approach distance have

$$\frac{\sigma_d}{d} = \frac{10^3}{11.1 \cdot 10^6} \frac{\mathrm{m}}{\mathrm{m}} = 9 \cdot 10^{-5} \tag{7}$$

for Pluto, and $\sigma_d/d = 3.7 \cdot 10^{-5}$ for Charon.

Again the error in the observed $(\Delta v)_\infty$ is of the order,

$$\frac{\sigma_{\Delta v}}{(\Delta v)_\infty} = \frac{0.02 \cdot 10^{-3}}{1.8} \frac{\mathrm{m\,s^{-1}}}{\mathrm{m\,s^{-1}}} = 1.1 \cdot 10^{-5} \tag{8}$$

for Pluto and $\sigma_{\Delta v}/(\Delta v)_\infty = 2.3 \cdot 10^{-4}$ for Charon.

For the values in Eqs. 6–8, the individual first order relative accuracy of GM is of the order of

$$\frac{\sigma_{\mathrm{GM}}}{GM} \approx 1 \cdot 10^{-4} \tag{9}$$

for Pluto and Charon. We note that the relative accuracy of the gravitational constant G is similar, $1.2 \cdot 10^{-4}$ (Woan, 2000).

As comparisons of the values found in Eqs. 6 and 8, with those of Eqs. 7 show, the major determinant of the accuracy of GM is the uncertainty in the distance of closest approach, d. A potentially better accuracy in the determination of $(\Delta v)_\infty$ would make the closest approach distance the sole driver of the GM accuracy. The reverse is also true, namely, any poorer knowledge of the closest approach distance than 1 km would worsen the accuracy of the derived GM values significantly. In principle, it should be possible to extract the individual masses of both bodies with an accuracy of

at least one to two orders of magnitude better than the current best values (see Table VII).

Referring again to Fig. 6, it is clear that since the total velocity signature is the sum of the individual velocity changes, that the key to separation of the velocity curves, and hence to separating the masses of Pluto and Charon, is the availability and quality of data that can be obtained in within an hour or two of the center of the encounter. The NH encounter addresses as prioritized list of objectives which in turn lead to specific observations at particular times in the encounter sequence. Since the HGA is body mounted, during the encounter the pointing of the antenna is controlled by the overall mission objectives since the specialized instruments are also body mounted. The amount of tracking that can be practically obtained then depends mostly on the occurrence of favorable opportunities to acquire tracking data. This has not be analyzed to date.

The radio occultation observations of Pluto and Charon provide two known opportunities to obtain tracking data since the HGA will be Earth pointed for fractions of an hour in each instance. These opportunities occur about 45 min and 1h 10 m following closest approach to Pluto, *v.* Fig. 6 and Tables IX and X. The number and timing of other opportunities to obtain additional tracking data during the encounter period cannot be predicted at this time.

Radio occultation measurements and camera observations of Pluto and Charon will constrain the radii. Due to their slow rotation, both bodies are expected to be close to spherical objects. The derived occultation radii alone is therefore expected to be representative of any chord passing through them. In any event, the best volume measurement will be derived from the combination of occultation and imaging constraints, thereby removing uncertainties in shape as a limitation on our knowledge of the bulk density. The relative accuracy of the bulk density for a radius accuracy as large as 1 km can be on the order of 10^{-3}, which is more than an order of magnitude more accurate than the densities known today and sufficient to distinguish between different models of the interior.

4. Radiometry

4.1. Surface Temperatures of Pluto and Charon

At those times when the New Horizons spacecraft high gain antenna (HGA) points toward Pluto or Charon, the REX instrument, operating in a "radiometry mode," will receive 7.2 GHz thermal radio emission from the two bodies. Opportunities to observe radio thermal emission occur during the several minutes of radio occultation measurements when the disks of Pluto

and Charon obscure the Earth. The REX instrument will detect radiation from the obscuring body as an increase in the radio system noise level in the radiometry channel and also an increase in the noise floor of the occultation channel. These observations will be used to derive the nightside emission temperatures of Pluto and Charon. It is possible that pointing maneuvers undertaken for other instruments will also sweep the HGA across Pluto and/or Charon.

For the nightside observations the New Horizons HGA will remain pointed in the Earth direction for the duration of the occultation events, beginning and ending well-above any anticipated sensible atmospheric and ionospheric effects. The motion of the spacecraft will scan the HGA beam across the surface of the planetary disk during the short interruption in uplink signal reception when NH is behind the occulted body. This strategy provides opportunities to determine the otherwise inaccessible nightside surface decimeter-emission temperatures. Supplementary observations are desired before and after the encounter in order to compare the conditions of the sunlit side under near-full-disk illumination with those of the nightside hemisphere.

The applicable REX instrument radiometric system parameters are given in Table VIII. Key geometric and sequencing parameters of this specific observation opportunity at Pluto and Charon are listed in Tables IX and X.

Table VIII. Instrumental Characteristics for REX Radiometry

wavelength λ	4.2 cm (X-band uplink, 7.1 GHz)
HGA diameter	2.1 m
HGA gain	41.9 dBi
HGA boresight offset	0.25° (4.4 mrad)
3 dB beam diameter	1.2° (20.9 mrad)
System temperature $T_{\rm sys}$	150 K
RF Bandwidth	250 MHz
IF Bandwidth	4.5 MHz
Polarization	RCP (Chan A)/LCP (Chan B)
$\Delta T_{\rm rms}$	70 mK (at $\tau = 1$ s)

As shown in Fig. 7, the HGA boresight follows the approximately diametric subspacecraft track across the disk of Pluto. As a result of the dominant component of spacecraft motion away from the Sun, the HGA beam on Pluto increases in size as it sweeps across the disk, but remains much smaller than the diameter of Pluto, taken as $2,330 \pm 30$ km (Tholen and Buie, 1997).

Under these conditions, it is possible to use the approximation that the receiver sky temperature approaches that of the Pluto nightside kinetic surface temperature to within a few percent. Minor corrections are required

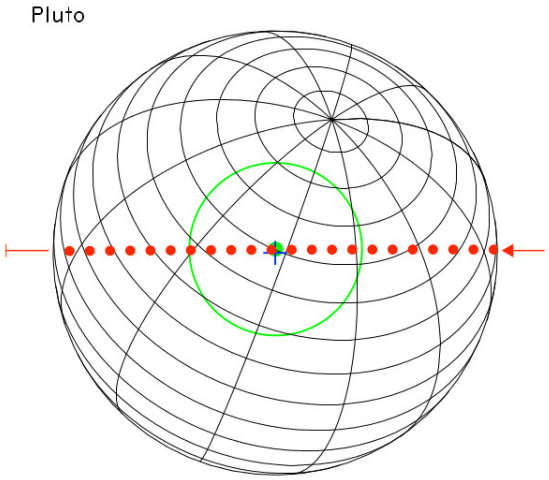

Figure 7. View of Pluto nightside from the NH spacecraft during Earth occultation on 14 July 2015. The virtual position of Earth, the nominal pointing target for the spacecraft HGA, is shown at 30-s intervals along the trajectory. The subspacecraft point on Pluto at mid-occultation is marked with a blue cross. The green dot and concenteric green circle mark the HGA boresight pointing position and 3-dB beam size on Pluto for the same instant of mid-occultation.

to account for the obscuration of the sun and antenna side lobe effects. Although Pluto is a relatively fast rotator, the high tilt of its rotation axis may lead to significant differences between the microwave surface temperature on the backside as compared with the sunward side. That is, the nightside could be distinctly cooler than the roughly 40±5 K derived in the late 1980s and early1990s from ground-based mm and far infrared observations of the sunlit hemisphere (Altenhoff et al., 1988; Jewitt, 1994; also see Tryka et al., 1994), and the more recent observations in the range of 54–63 K (Lellouch et al., 2000).

4.2. Thermal Emission Observations

During occultation ingress and egress, the radiative sky background will be dominated by the Sun at 32 AU. Assuming that the normalized solar flux F(1AU) = 70 × 10^4 Jy at $\lambda = 4.2$ cm, the sky temperature is computed to be $T_{\rm sky} \simeq 3$ K. This is only a small fraction the estimated overall system temperature $T_{\rm sys} \simeq 150$ K.

The sensitivity of the REX instrument for radiometry $\Delta T_{\rm rms}$ is usually expressed by the formula:

$$\Delta T_{\rm rms} = \frac{T_{\rm sys}}{\sqrt{\Delta f \tau}} \tag{10}$$

where Δf is the receiver bandwidth and τ is the integration time. Using the applicable IF-bandwidth of 4.5 MHz, the above formula yields a sensitivity in the neighborhood of $\Delta T \simeq 70$ mK for the emission temperature. Additional analysis of surface emissivity effects will be required to estimate the physical temperature. Knowing the temperature to this degree of accuracy is of interest because of its importance for the vapor pressure of gases in the nightside atmosphere (e.g., Cruikshank et al., 1997).

Geometrical conditions are not as favorable at Charon as those planned for Pluto, Fig. 8. As a result of the greater distance and smaller absolute disk size, the HGA beam always covers the entire disk of Charon. Nevertheless, the considerable differences in the surface properties derived for Pluto and

Charon would likely be manifested in different inherent emissivities and thus different nighttime temperatures (cite TBS/MB).

[[NOTE: Combine Pluto and Charon views on same plate?]]

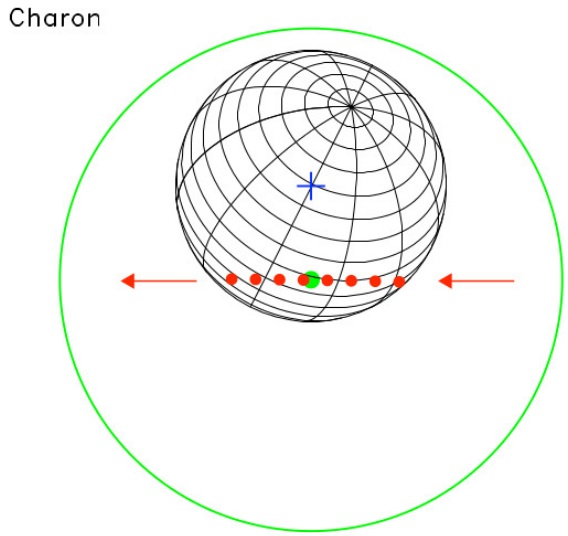

Figure 8. View of Charon nightside from the NH spacecraft during Earth occultation. See similar sketch of the Pluto occultation geometry for explanations of the various features. A major difference at Charon with respect to the Pluto occultation is that the 3-dB beam is now much larger than the Charon disk.

5. REX Implementation

5.1. IMPLEMENTATION-OVERVIEW

The 'Flight Element' of REX is economically based on the shared use of the onboard transceiver to provide reception, amplification, and filtering of the uplink signal from the ground to implement the scientific observations discussed above. Transfer of the signal tapped near the end of the amplification chain makes it possible for the essential process of sampling and the final signal conditioning and filtering needed to efficiently capture the information required for occultation and radiometry to be carried out with only a small amount of additional hardware.

As the signal used by REX are the same as those processed in the receiver for purposes of spacecraft tracking and commanding (Fig. 1 and accompanying discussion), the signal bandwidth presented to REX is optimized primarily for transceiver functions. This bandwidth represents a usable choice for radiometry, but is much greater than are required for the occultation experiment. Given the input constraints from the transceiver, the REX hardware implementation carries out two parallel processes: i) for radiometry, determination of the total noise power in the input stream to REX, which is proportional to the linear combination of 4.2 cm-λ noise entering the spacecraft antenna with that internally generated by the receiver,

Table IX. Pluto Encounter

Encounter Date	14 July 2014 at 11:59:00 SCET
Pluto Closest Approach (PCA)	11:59:00 SCET
Solar Distance	32.91 AU
Earth Distance	31.91 AU [near opposition]
Pluto Distance	11,095 km
Relative Velocity	13.78 km/s
Sun Occultation Entry	12:43:21 SCET (PCA + $44^{m}21^{s}$)
Earth Occultation Entry	12:44:05 SCET (PCA + $45^{m}05^{s}$)
Pluto Distance	38,895 km
Pluto Latitude	16.7°
Beam Diameter	814 km (0.35 D_{p})
Earth Occultation Midpoint	12:49:34 SCET (PCA + $50^{m}34^{s}$)
Pluto Distance	43,258 km
Pluto Latitude	50.1°
Beam Diameter	906 km (0.39 D_{p})
Sun Occultation Exit	12:54:10 SCET (PCA + $55^{m}10^{s}$)
Earth Occultation Exit	12:55:04 SCET (PCA + $56^{m}04^{s}$)
Pluto Distance	47,666 km
Pluto Latitude	−12.7°
Beam diameter	998 km (0.43 D_{p})
Duration of Occultation	$10^{m}59^{s}$ (659 s)

Table X. Charon Encounter

Encounter Date	14 July 2014
Charon Closest Approach	12:12:56 SCET (PCA + $13^{m}56^{s}$)
Solar Distance	32.91 AU
Earth Distance	31.91 AU [near opposition]
Charon Distance	26,925 km
Relative Velocity	13.88 km/s
Sun Occultation Entry	14:13:35 SCET (PCA + $2^{h}14^{m}35^{s}$)
Earth Occultation Entry	14:15:11 SCET (PCA + $2^{h}16^{m}11^{s}$)
Charon Distance	105,340 km
Charon Latitude	$-11.0°$
Beam Diameter	2,206 km (1.86 D_{c})
Sun Occultation Exit	14:16:40 SCET (PCA + $2^{h}17^{m}40^{s}$)
Earth Occultation Midpoint	14:17:12 SCET (PCA + $2^{h}18^{m}12^{s}$)
Charon Distance	106,965 km
Charon Latitude	$7.8°$
Beam diameter	2,240 km (1.89 D_{c})
Earth Occultation Exit	14:19:13 SCET (PCA + $2^{h}20^{m}13^{s}$)
Charon Distance	108,591 km
Charon Latitude	$-33.4°$
Beam diameter	2,274 km (1.92 D_{c})
Duration of Occultation	$4^{m}02^{s}$ (242 s)

and ii) for occultation data analysis and gravity, narrow-band filtering of the input signal to isolate the uplink signal and to reduce the retained bandwidth to the minimum required. In addition, REX hardware also handles the necessary housekeeping tasks needed to maintain the interface with the spacecraft onboard memory. Required inputs to the REX system are the USO-derived clock and the signal feed from the NH transceiver. We note that the REX hardware is integrated with the NH transceiver, and that the control actions necessary for REX are implemented as transceiver functions.

The inputs to the REX instrument are samples of a 4.5 MHz bandwidth transceiver IF channel sampled at the rate of 10 Ms/s. This input stream is processed to accomplish the two primary functions described above. In the first instance the processing consists of simple squaring and accumulation of the IF channel output. In the second instance the processing is based on a series of complex steps which begin with digitally translating the wideband input to baseband using a frequency reference derived from the NH USO. As indicated in Fig. 1, this processing takes place in a single field programmable gate array (FPGA), with spacecraft resource requirements as summarized in Table II. As a result of the complexity of the signal processing, the bulk of the FPGA capabilities as measured in the number of logic gates required and clock cycles to compute are dedicated to the coherent processing that captures the uplink occultation signal.

5.2. Extraction of Total Received Signal Power

Referring to the upper path within the dashed box, "FPGA," in Fig. 1 the REX power integrator follows the conversion of the uplink NH transceiver signal to 10 bit digital samples. These data are passed to the REX processor at a rate of 10 Ms/s, where they are processed to extract the total power in the input stream. This is accomplished by the simple expedient of squaring and adding, as

$$P_{\rm up}(k) = \sum_{i=N(k-1)+1}^{kN} s_i^2 \tag{11}$$

where, i is the index of the input samples from the quantizer, k is the number of the output sample, and N is the number of squared samples included in the average during each 0.1 s of observation time. In the REX realization $P_{\rm up}$ is represented by 40 bits. These power estimates are interleaved in the REX high-speed output stream and sent to the spacecraft solid state recorder (SSR).

5.3. Multiplierless, Anti-aliasing Filter Design

Referring to the lower path within the dashed box, "FPGA," in Fig. 9, the REX signal processor conditions the baseband signal by reducing the bandwidth to the near-minimum required to support the radio occultation experiment. As indicated above, this is accomplished by heterodyning to

zero frequency the uplink carrier signal centered initially at the 2.5 MHz IF center frequency, followed by use of time-invarient baseband filters to reduce the bandwidth. In designing the method of conversion to baseband frequencies from the IF channel, the precise frequencies and bandwidths of 4.5 MHz filter input and the REX processor channel were chosen to permit an efficient digital translation scheme represented schematically in Fig. 9. The process of down conversion is accomplished by first multiplying the wideband signal by the in-phase reference, i.e., a signal that is proportional to the cosine of the reference frequency, and a parallel multiplication by the quadrature reference, i.e., a signal that is proportional to the sine of the reference frequency.

The downconversion produces two components, one which is 'in-phase' with the USO-derived reference signal, the 'I' component, and the other 'in quadrature' with the USO-derived reference phase, the 'Q' component. At the same time, the center frequency of both components is shifted to 0 Hz (or 'DC'), from 2.5 MHz, by this process. The I,Q signal components are then filtered simultaneously by identical $\approx$ 1 kHz lowpass 'anti-aliasing' filters in order to suppress all but the central portions of the original IF spectrum, followed by decimation to the lower sampling frequency 2.441 kHz. Each anti-aliasing filter is implemented as a low power, 'multiplierless' decimation filter making use of the signal processing architecture described below. As noted above, all other mixing frequencies in the NH transceiver

are also derived from the same USO reference source as the REX processor, so that the fundamental frequency and phase stability of the system is set by the USO, and realized by the quality of the transceiver circuitry.

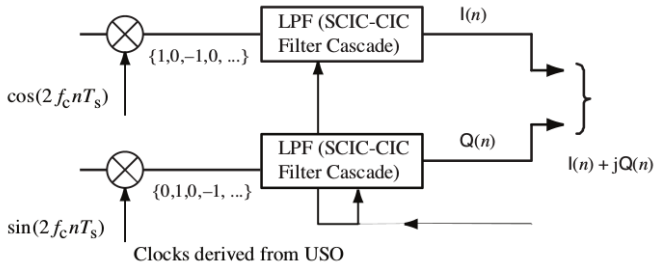

Figure 9. Block diagram of REX narrow band signal processing. An efficient means of heterodyning the wideband uplink signal to baseband is afforded by the choice of centering the wideband signal at 2.5 MHz, and using a 10 MHz reference frequency. The 1:4 ratio of these frequencies results in a multiplier sequence, shown in the figure just to the right of the multipliers, that in effect sends alternate ADC samples successively to the I and Q channels, where the sign is changed of every other sample in each channel. This simple prescription involves only a multiplexer and a switchable inverter, without need for the degree of precision and processor speed, or use complex multipliers required in a more conventional design.

In a digital implementation certain choices of the reference, or 'local oscillator' frequency lead to marked simplifications of digital processes. This characteristic of digital systems is exploited here by choosing the ratio of the center frequency of the wideband channel, $f_c = 2.5$ MHz , and the sampling frequency, f_s, to be 1:4, i.e.,

$$\frac{f_c}{f_s} = \frac{1}{4} \tag{12}$$

With four samples for each cycle of f_c the sequences of values for cosine and sine variations over a single cycle at the sampling frequency become '1, 0, -1, 0,' and '0, 1, 0, -1,' respectively, repeating infinitum. Consequently, the result of multiplication by cosine and sine at a frequency f_s can be implemented by simple sample selections and sign changes to the values of the signal at f_c.

The process used here is illustrated in the left hand side of Fig. 9. For our choice of frequency ratios the algorithm is implemented by selecting only the even or only the odd samples and reversing the sign of every other sample in the selected sequences, thus avoiding any requirement for multiplication.

The anti-aliasing filter itself is also based on a class of digital, linear phase finite impulse response (FIR) filters comprising a cascade of integrators and comb filters (Hogenauer, 1981; Kwentus et al., 1997). In the REX implementation neither the integrators nor the comb filters use hardware multipliers, and for this reason they are referred to as 'multiplierless.' In particular, the transfer function of the integrators is,

$$H_I(z) = \frac{1}{1 - z^{-1}} \tag{13}$$

and comb filters with transfer function

$$H_C(z) = 1 - z^{-1} \tag{14}$$

Such filters can be realized by highly efficient and well-understood digital processes. The standard approach, however, results in filter pass band

characteristics that result in levels of out-of-band signal rejection that are deleterious to the REX design. To understand this, consider that the input noise to the digital filter spans 4.5 MHz, while the desired output bandwidth is only ≈1 kHz. As a result of sampling and signal decimation, noise that was initially well controlled at the higher, 10 Ms/s rate is 'folded' about 20,000 times when the sampling rate is reduced to 2.4 kHz. Thus, narrow band digital filter must have extremely low out-of-band response.

For REX, this problem has been solved, uniquely we believe, by modification of the standard "integrator and comb" filter to further suppress the filter side band responses. The resulting total out-of-band noise suppression achieved is noted in Table II. Details of the algorithm employed are given in the Appendix.

6. REX Commissioning

6.1. Purpose

In the months immediately following launch, the New Horizons project initiated a series of 'commissioning' activities designed to verify instrumental functionality and to measure the performance of the instrument complement. Commissioning of the REX instrument began with an initial test on April

19, 2006, while the spacecraft was still spinning following launch, designed to determine basic functionality and performance. This test included the exercise of calibration test patterns, the reception of an uplink signal transmitted by a DSN ground station for specific evaluation of the inflight REX system gain, linearity, stability of the composite uplink, USO, and REX receiver chain, characterization of the REX bandpass frequency response, and identification of the presence of spurious signals, if any, in the REX passband. These tests were repeated on June 1, 2006 with the spacecraft attitude stabilized on three axes. Two additional commissioning tests with three-axis attitude stabilization were conducted on June 20 and 29, 2006, for the purpose of measuring the beam pattern of the spacecraft high gain antenna (HGA), and for calibrating the REX system noise figure and radiometric sensitivity. We discuss the results of these tests, including a synopsis of the REX commissioning data, in the following sections.

6.2. Functional Verification

In addition to its operational connection to the NH transceiver, the input to the REX signal processor can be commanded to process a set of internal test patterns stored in the REX signal processor. The test pattern input sequences comprise an impulse response, three square waves of different frequencies, two pseudo-random number sequences that differ only in their

amplitudes, and a sequence containing only zeros. The response of the REX signal processor to each of these test patterns is fully deterministic, thus the REX output for each of the test pattern inputs can be compared with the expected response sample-by-sample, and bit-for-bit. Each time the REX processor is enabled in the NH transceiver, the first part of the test executes a subset of the test patterns for functional verification. For the commissioning tests the subset selected is: all zeros, impulse excitation, low-frequency square wave, full-scale pseudo-random sequence, and a repeat of the all-zeros sequence. Each of these test patterns is enabled for six frames, or approximately six seconds, during which the REX output is recorded in the spacecraft solid state recorder (SSR). After the REX contents of the SSR are transmitted to Earth, the REX data are compared with the expected test pattern response on a sample-by-sample and bit-for-bit basis. In all cases, the test pattern outputs matched precisely the expected response for each of the Commissioning tests and for each of the test patterns, thereby certifying the functionality of the REX signal processor.

6.3. Evaluation of Spurious Responses, No Uplink

A major concern in the design of the REX system, including its integration with the spacecraft transceiver, was to avoid the introduction of spurious receiver responses into the REX output. In practical terms the design crite-

rion adopted was that the strength of any spurious signals within the REX passband would be at least −55 dB-Hz below the planned uplink signal transmitted from the ground. The REX commissioning test to certify that this criterion had been satisfied placed the receiver in REX mode, selected the transceiver ADC source for REX and recorded REX data for 100 seconds. Then, in post-processing on the ground, frequency power spectra were computed for each of 100 frames, i.e., to 1 Hz resolution, and averaged over the 100 frames. The resulting test spectra were inspected for the presence of spurious responses. No such responses were observed with strength greater than five sigma above that of the spectrum noise floor, where for REX spectra the 5-σ level is −65 dB relative to the uplink signal strength. Thus, the spurious signal design criterion of −55 dB-Hz has been met in flight.

6.4. Uplink Signal Acquisition

The radio occultation experiment to probe the structure of Pluto's atmosphere requires that REX instrumentation support acquisition of an uplink signal-to-noise ratio (SNR) of at least 55 dB-Hz, anywhere within an approximately 1-kHz band centered on the planned frequency of the uplink signal. At a nominal distance to Pluto of 40 AU, the SNR requirement is met by transmitting approximately 10 kW at a frequency of 7.2 GHz from one or more 34-m DSN antenna to the spacecraft resulting in an absolute

uplink power in the NH transceiver radiometric channel of −110 dBm. The 55 dB-Hz criterion can be achieved, for example, if the noise floor in the REX spectrum is −170 dBm-Hz or less, and the spurious-free dynamic range (SFDR), is 55 dB-Hz or better. Then at Pluto, the uplink SNR will be 55 dB-Hz or more and adequate to meet the sensitivity requirement of the radio occultation uplink experiment.

To verify that REX has adequate sensitivity the REX commissioning tests emulated the expected uplink signal strength at 40 AU by reducing the transmitted power from the DSN to a level which resulted in a signal strength of −110 dBm in REXs baseband channel. We used data obtained under the conditions just described to quantify the uplink signal strength, the SFDR, and the level of the noise floor. For this purpose we calculated the frequency spectra of the REX data with a frequency resolution of 1 Hz. Figure 10 shows an average of 100 such spectra obtained from the REX data during the commissioning tests, showing the uplink signal somewhat stronger than the −110 level expected at Pluto encounter, at −105 dBm in 1-Hz bins. The noise floor at −171 dBm-Hz, is somewhat lower than pre-flight tests. At the same time the spectrum is free of spurs to better than −65 dB, except for a feature located at a frequency of 60 Hz and its harmonics, which were not evident in the no-uplink acquisitions. The absence of these features when no uplink signal was present and their occurrence as harmonics of the

DSN station line power frequency indicates that these features originate as low-level modulation products in the ground transmitter.

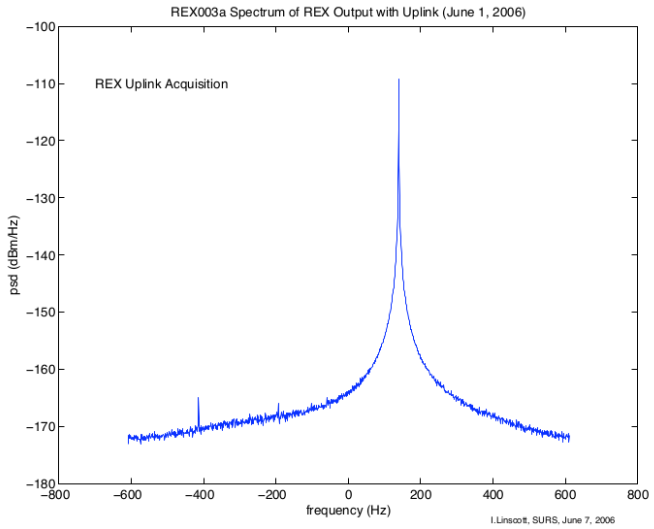

Figure 10. Uplink Signal in REX. Spectrum of received uplink signal, transmitted by the DSN and acquired in the NH REX radiometric channel during commissioning tests. Spectrum was computed from REX output data to a resolution of 1 Hz, and is the average of 100 unwindowed FFTs. The sprectum shows the uplink at +135 Hz offset from the expected received frequency. The spurious responses at ≈ 200 and 400 Hz are harmonics of 60 Hz, and believed to be modulation artifacts from the ground-based X-band transmitter.

6.5. USO Stability

Over the course of the REX Commissioning the uplink was transmitted CW, with the radiated frequency adjusted for Doppler shifts associated with the Earth and spacecraft in order to control the received frequency at NH.

Signal acquisitions by REX spanned periods of typically 100 seconds, but occasionally lasting up to 1000 seconds. For these acquisitions the frequency of the acquired signal in the REX channel can be estimated with a precision limited by the signal SNR, typically +60 dB-Hz. This corresponds to a lower bound of about 0.001 Hz, using REX spectra with 1-Hz resolution. A sample profile of frequency estimates of the uplink signal is presented in Fig. 11. The top plot of the pair shows a series of frequency estimates obtained each 0.2 s during the 100 seconds spanning the REX output. In this interval the frequency drifted upward at a nearly linear rate over the entire100 seconds of the observation. Removing the trend to second order, leaves residuals with a standard deviation of 0.0078 Hz, for the 0.2 second window. Expressing this deviation relative to the nominal received frequency of $7.2 \cdot 10^9$ corresponds to a fractional deviation over 0.2 sec of about 10^{-12}. Repeating the estimates using sampling intervals of 1 and 10 s, respectively, results in variations of $5 \cdot 10^{-13}$ in 1 s and $1.4 \cdot 10^{-13}$ in 10 s, suggesting that the USO on transceiver Side A is approaching the stability required for the radio occultation experiment at Pluto. (No data are available as of this writing for the second USO on Side B.)

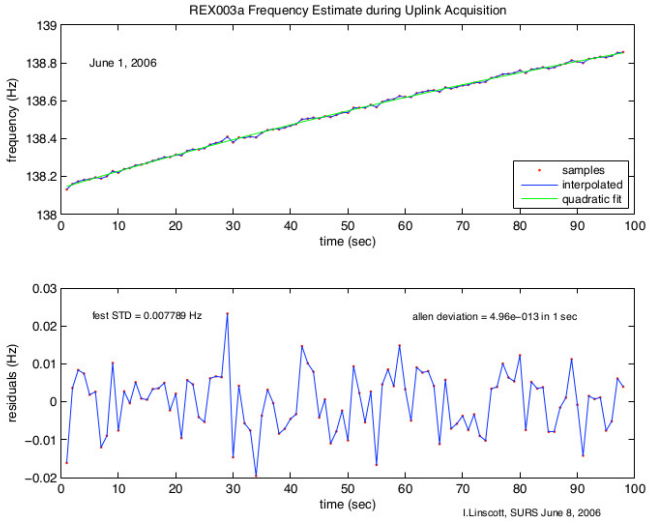

Figure 11. REX estimates of uplink frequency. Upper plot gives the estimated frequency profile obtained using a 0.2 Hz frequency analysis window sequentally over a 100 s duration REX data set, showing a nearly linear upward drift. Removing the trend to second order leaves residuals in lower plot, with a standard deviation of 0.0078 Hz for the 0.2 second window. Allan deviation at 0.2 sec interval is $\approx 10^{-12}$, relative to the 7.2 GHz uplink frequency. Estimates using durations of 1 and 10 s respectively result in corresponding Allan deviations of $5 \cdot 10^{-13}$ and $1.4 \cdot 10^{-13}$, respectively. Results are from transceiver "Side A."

6.6. REX Passband

In order to measure the in-flight response of the REX narrow band filter, the uplink signal frequency was swept slowly across the REX passband during REX Commissioning on April 19 and again on June 20, 2006. In the April 19th test, during which the spacecraft was in its spin-stabilized attitude control mode, a small sinusoidal variation of ± 0.5 dB was observed in the

received power at the spin frequency. This is attributed to a slight misalignment of the spacecraft spin axis with the HGA's boresight. We compensated for this effect by modeling the power variations and removing the effect of the spin from the data. Figure 12 shows the REX bandpass sweep response where both the uncompensated response and the adjusted response using the sinusoidal model are included. The side lobes of the REX lowpass filter appear at frequencies of about ±1.8 kHz, where the relative signal level of −44 dB, which is consistent with the filter design. The swept response is correctly symmetric, and the noise level drops to a minimum at ±3 kHz, which is the location of the multiplierless FIR filter nulls.

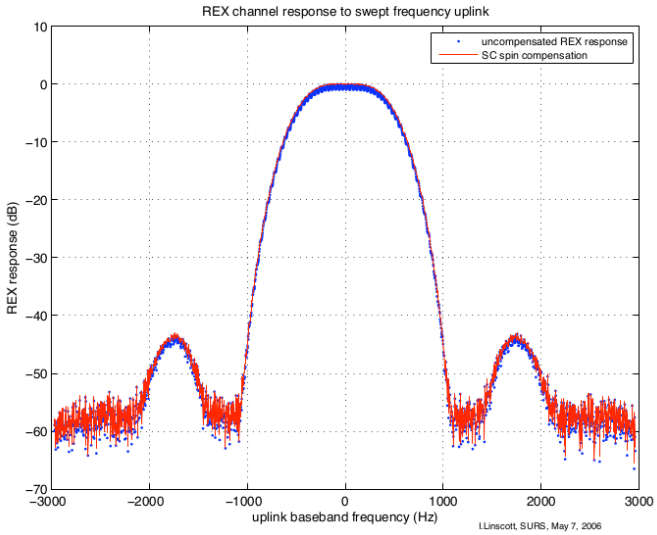

Figure 12. REX Uplink Passband. Response of REX slow frequency sweep across passband. Shown are both the response in blue uncompensated for spacecraft spin, and in red the response using a sinusoidal modulation model to correct for the spacecrafts spin.

6.7. HGA Beam Pattern

The REX commissioning test on July 20, 2006 was dedicated to mapping the beam pattern of the NH spacecraft high gain antenna. We obtained the beam pattern by tuning the frequency of an unmodulated uplink signal of constant power from the DSN to arrive at the NH spacecraft with a constant frequency; the signal served as a calibration source. At the same time, we varied the spacecraft attitude with respect to the direction to Earth, thus implementing a scan of the HGA beam over a small range of angles about the Earth direction, centered approximately on the beam maximum. The initial offset of the scan was set at the upper left corner of a 2° x 2° angular box. The beam direction then was made to "nod and step" parallel to the box edges so as to perform a raster scan about the Earth direction. During the scan the transceiver captured the uplink signal in REX mode, with the REX output recorded and time-tagged onboard. At the same time the spacecraft body vectors were logged and time-tagged. The combination of these two time sequences allowed us to map estimates of the uplink signal power to the spacecraft pointing direction.

The resultant HGA response is shown in Fig. 13. An approximately 0.2° offset of the HGA response apparent in the figure is believed to be the result of a shift in the center of mass of the spacecraft from the pre-launch condition, a likely consequence of the redistribution of fluid in the fuel tanks.

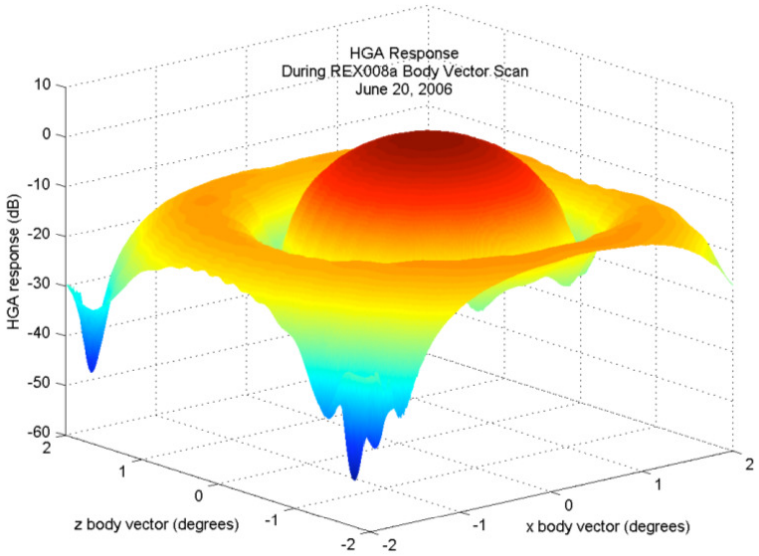

Figure 13. New Horizons High Gain Antenna beam pattern at 7.2 GHz. Response to NH HGA to an uplink signal as the spacecraft is scanned raster-like over a 2° x 2° region. Actual center of beam is offset ≈ 0.2° from Earth direction, in $+x$ direction.

6.8. Radiometer Calibration

On June 29, 2006, while in REX mode, we obtained a series of five crossed scans of radio astronomy sources together with dwells on cold sky. The spacecraft HGA was initially commanded to point at an offset from the source direction of $-1°$ along the NH body coordinate x, and then scanned across the source at 100 μrad/sec to $x = +1°$, a maneuver that required approximately 350 s. Similar scans were performed for the vertical, or z-coordinate, but with a dwell of 300 s at the origin $x = z = 0$.

The radiometer function in REX integrates the power in data samples from the wideband, 4.5 MHz radiometric channel (*v.* Section 5.2). The ac-

cumulated growth of the integrated value is placed in the REX high-speed data stream 10 times per second, and the accumulator is reset every 1.024 seconds, i.e., on the REX frame boundaries. The horizontal scans obtained for the radio source Cygnus-A are shown in Fig. 14, normalized to the cold-sky power level. The 1-s samples have been smoothed using a 10-s sliding window. Scans of Cassiopia-A are similar.

The standard deviation of the 10-s averages indicates that the NH transceiver is radiometrically stable at a level of approximately 5 parts in 10,000, and thus adequate for measuring radiometric temperature to a precision of 0.1 K, or about 1 part in 1000.

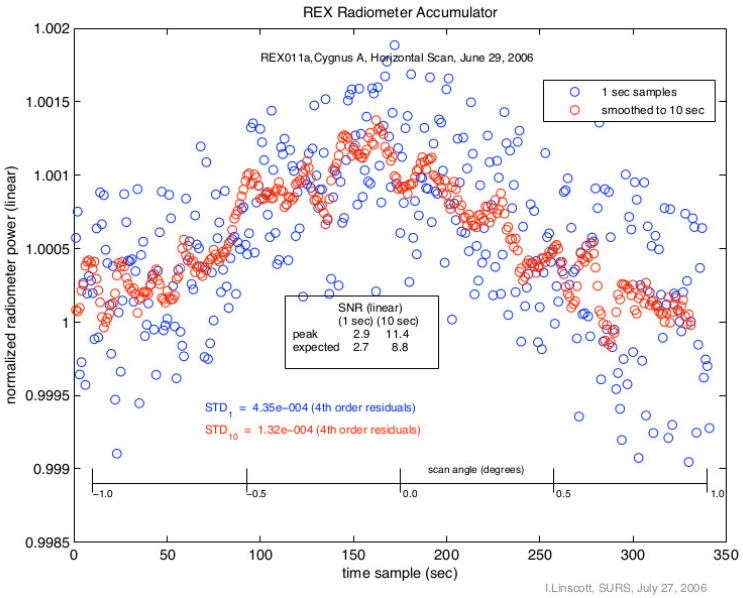

Figure 14. REX Scans of Cygnus-A. Values of REX radiometer accumulator is plotted vs scan angle. Both one second (blue), and 10 second (red), averages are included.

7. Summary

Planned New Horizons REX observations of Pluto and Charon, discussed above, address directly our goals for increased understanding of this interesting system: *i*) measurement of atmospheric conditions near and at the surface of Pluto for determination of surface conditions and the possible observation of ionospheres at Pluto and Charon; *ii*) an independent determination of the Pluto-Charon system mass, as well as an independent determination of the Pluto-Charon mass ratio,; *iii*) nightside observations of the thermal emission from Pluto and Charon with sufficient resolution to determine the brightness distribution across the disk of Pluto; *iv*) expected improvements in the densities of Pluto and Charon from the radio occultation chord in combination with other NH observations, and from expected improvements in the mass of Charon.

In addition, the New Horizons mission has the potential to observe the anomalous accelerations known as the Pioneer effect.

The Radio Experiment is poised to investigate a number of Pluto Science Definition Team Category I, II, and III science questions in the Pluto system, and to also address additional questions susceptible to radio tracking and propagation methods. Practical implementation of these investigations is made possible by close cooperation between the REX science team, the designers and implementers of the spacecraft radio transceiver system, and

the NASA Deep Space Network. With the New Horizons Mission successfully in flight operations the science goals set for REX are within reach.

Acknowledgements. This work is carried out as part of the New Horizons Radio Science investigation or Radio Experiment (REX). In the U.S. REX is supported by the National Aeronautics and Space Administration through the New Horizons Project at the Southwest Research institute. This paper presents results of a research project partially funded by the Deutsches Zentrum für Luft-und Raumfahrt (DLR). We thank the Radio Frequency Engineering Group in the Space Department at APL for their collaboration and critIcal contributions to the realization of the REX instrument.

Appendix

System Function of the SCIC Filter

A. Theory of the CIC-SCIC Filter

A.1. Cascade Integrator Comb (CIC) Filter

Referring to the material introduced in Subsection 5.3, Hogenauer (1981) proposed use of a cascade of N stages of integrators operating at a sampling frequency, f_s , and comb filters operating at a lower sampling frequency f_s/R . Such a combination, called a "cascaded integrator comb filter," or CIC, has the following transfer function,

$$H_{\mathrm{CIC}}(z) = H_I^N(z) H_C^N(z) = \left(\frac{1 - z^{-RM}}{1 - z^{-1}} \right)^N = \left[\sum_{k=0}^{RM-1} z^{-k} \right]^N \tag{15}$$

where the factor, R, is the decimation ratio of the input to the output sampling frequencies. As revealed in the form of the transfer function, the CIC is a series of N identical FIR filters. A CIC is represented schematically in Fig. 15.

The frequency response of the above filter derived from the transfer function is,

$$H_{\mathrm{CIC}}\left(e^{j\omega}\right) = \left\{ \frac{\sin \frac{\omega RM}{2}}{\sin \frac{\omega}{2}} e^{-j\omega\left[\frac{RM-1}{2}\right]} \right\}^N \tag{16}$$

The CIC frequency response, Eq. 16, is characterized by a sequence of nulls at multiples of $f = 1/M$, where M is the integrator depth, chosen to control the placement of the nulls. The design is such that the location of the nulls when aliased fold back onto DC, then the aliasing near DC is

substantially suppressed. For REX observations the uplink signal will be placed in frequency near $f_s = 2.5 + \Delta$ MHz, where typically $|\Delta| \approx 10^2$ Hz. With $f_c = 10$ MHz and $\frac{f_c}{f_s} = 1/4$, use of the receiver architecture in Fig. 9 results in the uplink signal appearing at frequency Δ relative to DC. For these choices the nulls of the CIC filter strongly suppress aliased out-of-band signal components. In the REX CIC the decimation ratio is $R = 4096$, i.e., 10MHz/4096 = 2.441 KHz. The transfer function in equation (15) indicates that the CIC filter produces a gain of $(RM)^N$ at DC, which has serious implications for precision at high values of R. Additionally, the CIC filter has the disadvantage of affording little choice in the filter response characteristics. These limitations are addressed by splitting the decimation factor in two parts $R = 4096 = 64 \cdot 64$. The first decimation factor is realized in a traditional CIC filter. The second factor, or stage is implemented in a sophisticated modification of the CIC filter, called a 'Sharpened CIC' filter. As discussed in Hogenauer (1981) the efficiency of the overall design arises from the attributes that: i) it requires no multipliers and, ii) the second cascade of comb filters operates at the lower data rate, resulting in substantial power savings. The simplicity of the corresponding physical structure makes it appropriate for hardware implementation in an FPGA.

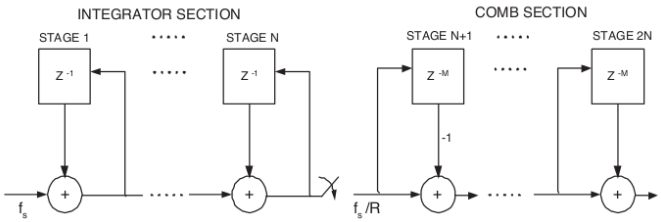

Figure 15. Schematic block diagram of the multiplierless CIC architecture.

A.2. Sharpened CIC filter

The sharpened CIC, or SCIC, filter was first proposed by Kwentus et al. (1997), based on an earlier suggestion by Kaiser and Hamming (1977), as a method to overcome a rather significant drop off in the passband that is characteristic of the standard CIC filter. As it happens, use of the SCIC architecture improves the out-of-band response as well, relative to the CIC design. A schematic representation of the SCIC filter is shown in Fig. 16. The response of the SCIC filter is,

$$\begin{aligned} H_{\mathrm{SCIC}}(z) &= H^2_{\mathrm{CIC}}(z)\left[3z^{(\frac{RM-1}{2})N} - 2H_{\mathrm{CIC}}(z)\right] \\ &= \left(\frac{1-z^{-RM}}{1-z^{-1}}\right)^{2N}\left[3z^{-(\frac{RM-1}{2})N} - 2\left(\frac{1-z^{-RM}}{1-z^{-1}}\right)^{N}\right] \quad (17) \end{aligned}$$

In particular, for the REX implementation, $R = 64, M = 1, N = 2$, the frequency response of the SCIC filter is shown in Fig. A.3.

The CIC-SCIC retains the advantage of having nulls at multiples of $f = 1/M$, while achieving a steeper drop at the band edge response than in the CIC filter.

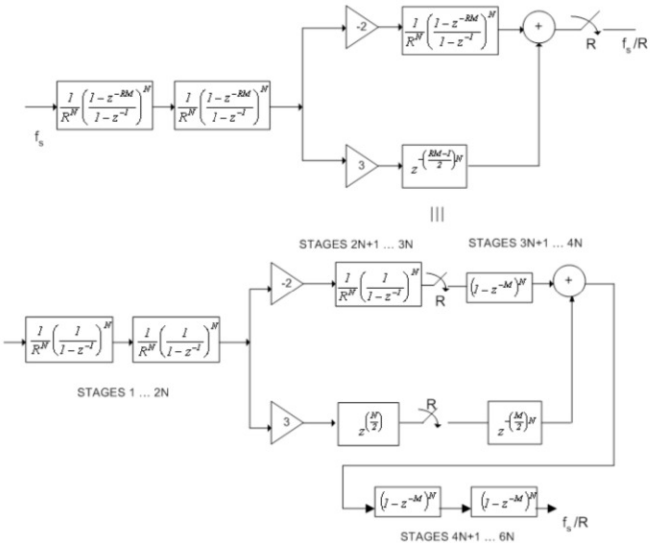

Figure 16. Schematic block diagram of the multiplierless SCIC architecture.

A.3. Lowpass, Anti-aliasing Filter Design

A high precision implementation of a staged CIC-SCIC filter involves careful design of register length along the data path in the two filters. To do so requires modeling and simulation of the growth of errors due to truncation or rounding along the data path, as there is no analytic solution to the problem. The visibility afforded by this approach makes is possible to optimize the allocation of precision along the processing path.

The precision in CIC and SCIC filters is determined by the overall register growth, combined with a truncation principle that accounts for the propagation of quantization errors along the data path of the filter. By combining register growth with truncation, a worst-case design principle is established

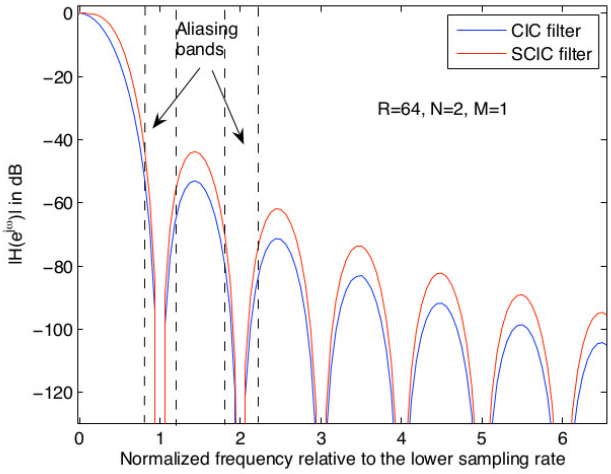

Figure 17. Frequency response of SCIC and CIC filters. Frequency response of SCIC and CIC filter. Note increased sharpness of the SCIC nulls in the aliasing bands as compared with the CIC realization. SCIC filter also has the flatter passband and sharper transition

where the truncation error at the filter's output uniformly bounds the error incurred at the intermediate stages. Specifically, drawing from the discussion by Hogenauer (1981), if B_j denotes the number of bits truncated at the j^{th}-stage, $j = 1, \cdots, 6N$, for the SCIC filter as shown in Fig. 16, the truncation error has a uniform distribution with a width of

$$E_j \;=\; \begin{cases} 0, & \text{in the absence of truncation or rounding} \\ 2^{B_j}, & \text{otherwise} \end{cases} \tag{18}$$

The mean and variance of the error sources at the j^{th}-stage are given by

$$\mu_j \;=\; \begin{cases} \frac{1}{2}E_j, & \text{if truncation is applied} \\ 0, & \text{otherwise} \end{cases} \tag{19}$$

and the variance of the error is

$$\sigma_j^2 = \frac{1}{12} E_j^2 \tag{20}$$

Further, let h_j denote the impulse response of the system function of the j^{th}-stage up to and including the last stage. The functional representation of h_j is derived and discussed in detail in the appendix. The error introduced at the j^{th}-stage propagates to the output shaped by the impulse response, h_j. In particular, the mean of the error at the output of the SCIC filter due to truncation at the j^{th}-stage is

$$\mu_{T_j} = \mu_j D_j \tag{21}$$

where

$$D_j \;=\; \begin{cases} \sum_k h_j(k), & j = 1, \cdots, 6N \\ 1, & j = 6N+1 \end{cases}$$

is the "mean error gain" for the j^{th} error source due to truncation. Similarly, the variance at the output of the SCIC due to truncation at the j^{th}-stage is

$$\sigma_{T_j}^2 = \sigma_j^2 F_j^2 \tag{22}$$

where the sub-T stands for "total' and

$$F_j^2 \;=\; \begin{cases} \sum_k h_j^2(k), & j = 1, \cdots, 6N \\ 1, & j = 6N+1 \end{cases}$$

is the "variance error gain" corresponding to the j^{th} error source. Consequently, the total mean and variance of the error at the output are given

by

$$\mu_T = \sum_{j=1}^{6N+1} \mu_{T_j} \tag{23}$$

$$\sigma_T^2 = \sum_{j=1}^{6N+1} \sigma_{T_j}^2 \tag{24}$$

Based on Eqs. 23 and 24, the design criterion for the register length of each of the $6N$ filter stages is:

i) Make the variance due to truncation of the first 6N error sources at least as small as the error introduced by truncating the output.

ii) Distribute the accumulating truncation error equally among the first 6N sources.

Use of these criteria implies,

$$\sigma_{T_j}^2 \leq \frac{1}{6N}\sigma_{T_{6N+1}}^2, \quad j = 1, \cdots, 6N \tag{25}$$

and that,

$$\sigma_{T_j}^2 = \frac{1}{12}2^{2B_j}F_j^2 \tag{26}$$

where B_j is the number of bits truncated at stage j from the maximum register length, $B_{\max}$, which is itself a function of the inherent gain of the filter. The filter gain for the SCIS filter is,

$$G_{\max} = \sum_{k=0}^{3(RM-1)N} |h_1(k)| \tag{27}$$

It can be seen from Eq. 27 that $G_{\max} = (RM)^{3N}$ corresponding to the gain in the path that includes the additional CIC block. Hence,

$$B_{\max} = \lceil 3N \log_2 RM + B_{\text{in}} - 1 \rceil \tag{28}$$

where B_{in} is the number of bits to the input of the SCIC filter. Combining (26) through (28),the precision of the j^{th} filter stage in the REX implementation is,

$$B_j \leq -\log_2 F_j + \log_2 \sigma_{T_{6N+1}} + \frac{1}{2} \log_2 \frac{2}{N} \tag{29}$$

It is clear from Fig. 16 and equation (17) that the transfer function from the j^{th}-stage up to and including the last stage is given by,

$$H_j(z) = \begin{cases} H_I^{2N-j+1} \left[3z^{-\left(\frac{RM-1}{2}\right)N} - 2H_C^N H_I^N \right] H_C^{2N}, & j = 1, \cdots, 2N \\ -2H_C^{3N} H_I^{3N-j+1}, & j = 2N+1, \cdots, 3N \\ H_C^{6N-j+1}, & j = 3N+1, \cdots, 6N \end{cases} \tag{30}$$

Expanding the terms,

$$H_j(z) = \begin{cases} \left(\frac{1}{1-z^{-1}}\right)^{2N-j+1} \left(1 - z^{-RM}\right)^{2N} \times \\ \qquad \left[3z^{-\left(\frac{RM-1}{2}\right)N} - 2\left(\frac{1-z^{-RM}}{1-z^{-1}}\right)^N \right], \\ \qquad\qquad\qquad\qquad\qquad\qquad j = 1, \cdots, 2N \\ -2\left(1 - z^{-RM}\right)^{3N} \left(\frac{1}{1-z^{-1}}\right)^{3N-j+1}, \\ \qquad\qquad\qquad\qquad\qquad\qquad j = 2N+1, \cdots, 3N \\ \left(1 - z^{-RM}\right)^{6N-j+1}, \\ \qquad\qquad\qquad\qquad\qquad\qquad j = 3N+1, \cdots, 6N \end{cases} \tag{31}$$

For an even number of cascade stages, N, let $N = 2P$,

$$H_j(z) = \begin{cases} H_j^0(z) = 3z^{-(RM-1)P}\left(\frac{1}{1-z^{-1}}\right)^{2N-j+1}\left(1-z^{-RM}\right)^{2N} \\ \qquad\qquad - 2\left(\frac{1-z^{-RM}}{1-z^{-1}}\right)^{N}\frac{\left(1-z^{-RM}\right)^{2N}}{\left(1-z^{-1}\right)^{2N-j+1}}, \\ \qquad\qquad\qquad\qquad j = 1,\cdots,2N \\ H_j^1(z) = -2\left(1-z^{-RM}\right)^{3N}\left(\frac{1}{1-z^{-1}}\right)^{3N-j+1}, \\ \qquad\qquad\qquad\qquad j = 2N+1,\cdots,3N \\ H_j^2(z) = \left(1-z^{-RM}\right)^{6N-j+1}, \\ \qquad\qquad\qquad\qquad j = 3N+1,\cdots,6N \end{cases} \tag{32}$$

We address each of the individual cases, $H^0(z)$, $H^1(z)$ and $H^2(z)$ individually to derive the corresponding impulse response values.

First consider $H^0(z)$, and let $H_j^0(z) = X_j^{00}(z) - X_j^{01}(z)$, where

$$X_j^{00}(z) = 3z^{-(RM-1)P}X_j^{00'}(z) \tag{33}$$

$$X_j^{00'}(z) = \left(\frac{1}{1-z^{-1}}\right)^{2N-j+1}\left(1-z^{-RM}\right)^{2N} \tag{34}$$

$$X_j^{01}(z) = \left(\frac{1-z^{-RM}}{1-z^{-1}}\right)^{N}\frac{\left(1-z^{-RM}\right)^{2N}}{\left(1-z^{-1}\right)^{2N-j+1}} \tag{35}$$

Manipulating the middle expression above for $X_j^{00'}(z)$,

$$\begin{aligned} X_j^{00'}(z) &= \left(\frac{1}{1-z^{-1}}\right)^{2N-j+1}\left(1-z^{-RM}\right)^{2N} \\ &= \left(1-z^{-RM}\right)^{j-1}\left(\frac{1-z^{-RM}}{1-z^{-1}}\right)^{2N-j+1} \\ &= \left(1-z^{-RM}\right)^{j-1}\left[\sum_{k=0}^{RM-1} z^{-k}\right]^{2N-j+1} \end{aligned} \tag{36}$$

$$= \sum_{k=0}^{2N(RM-1)+j-1} \left[\sum_{l=0}^{\lfloor \frac{k}{RM} \rfloor} (-1)^l \binom{2N}{l} \binom{2N-j+k-RM\,l}{k-RM\,l} \right] z^{-k}$$

This can also be written as a single sum,

$$x_j^{00'}(k) = \sum_{l=0}^{\lfloor \frac{k}{RM} \rfloor} (-1)^l \binom{2N}{l} \binom{2N-j+k-RM\,l}{k-RM\,l}, \quad k = 0, \cdots, 2N\,(RM-1)+j-1 \tag{37}$$

Then, since, $X_j^{00}(z) = z^{-(RM-1)P} X_j^{00'}(z)$, we have,

$$x_j^{00'}(k) = x_j^{00}\,[k-(RM-1)P] \tag{38}$$

Repeating this approach for $X_j^{01}(z)$,

$$\begin{aligned}
X_j^{01}(z) &= \left(\frac{1-z^{-RM}}{1-z^{-1}}\right)^N \frac{\left(1-z^{-RM}\right)^{2N}}{\left(1-z^{-1}\right)^{2N-j+1}} \\
&= \left(\frac{1-z^{-RM}}{1-z^{-1}}\right)^{3N-j+1} \left(1-z^{-RM}\right)^{j-1} \\
&= \left[\sum_{k=0}^{RM-1} z^{-k}\right]^{3N-j+1} \left(1-z^{-RM}\right)^{j-1} \\
&= \left[\sum_{l=0}^{3N} \binom{3N}{l} (-1)^l z^{-RM\,l}\right] \left[\sum_{\nu=0}^{\infty} \binom{3N-j+\nu}{\nu} z^{-\nu}\right] \\
&= \sum_{l=0}^{3N} \sum_{\nu=0}^{\infty} (-1)^l \binom{3N}{l} \binom{3N-j+\nu}{\nu} z^{-(RM\,l+\nu)} \\
&= \sum_{k\geq 0} \left[\sum_{l=0}^{\lfloor \frac{k}{RM} \rfloor} (-1)^l \binom{3N}{l} \binom{3N-j+k-RM\,l}{k-RM\,l}\right] z^{-k}
\end{aligned} \tag{39}$$

But,

$$\begin{aligned}
X_j^{01}(z) &= \frac{\left(1-z^{-RM}\right)^{3N}}{\left(1-z^{-1}\right)^{2N-j+1}} \\
&= \sum_{k=0}^{3(RM-1)N+j-1} x_j^{01}(k) z^{-k}
\end{aligned}$$

Hence, the range of k is established to be $k = 0, 1, \cdots, 3(RM-1)N + j - 1$ giving,

$$x_j^{01}(k) = \sum_{l=0}^{\lfloor \frac{k}{RM} \rfloor} (-1)^l \binom{3N}{l} \binom{3N - j + k - RM\,l}{k - RM\,l} \tag{40}$$

Putting this all together,

$$h_j^0(k) = \begin{cases} \sum_{l=0}^{\lfloor \frac{k}{RM} \rfloor} (-1)^l \binom{3N}{l} \binom{3N-j+k-RM\,l}{k-RM\,l}, \\ \qquad\qquad k = 0, 1, \cdots, \frac{(RM-1)N}{2} \\ \sum_{l=0}^{\lfloor \frac{k}{RM} \rfloor} (-1)^l \left[\binom{3N}{l} \binom{3N-j+k-RM\,l}{k-RM\,l} + \binom{2N}{l} \binom{2N-j+k-RM\,l}{k-RM\,l} \right], \\ \qquad\qquad k = \frac{(RM-1)N}{2} + 1, \cdots, 2(RM-1)N + j - 1 \\ \sum_{l=0}^{\lfloor \frac{k}{RM} \rfloor} (-1)^l \binom{3N}{l} \binom{3N-j+k-RM\,l}{k-RM\,l}, \\ \qquad\qquad k = 2(RM-1)N + j, \cdots, 3(RM-1)N + j - 1 \end{cases} \tag{41}$$

Similarly,

$$\begin{aligned} H_j^1(z) &= \left(\frac{1}{1 - z^{-1}} \right)^{3N-j+1} \left(1 - z^{-RM}\right)^{3N} \\ &= \left(1 - z^{-RM}\right)^{j-1} \left(\frac{1 - z^{-RM}}{1 - z^{-1}} \right)^{3N-j+1} \\ &= \left(1 - z^{-RM}\right)^{j-1} \left[\sum_{k=0}^{RM-1} z^{-k} \right]^{3N-j+1} \\ &= \sum_{k=0}^{3(RM-1)N+j-1} \left[\sum_{l=0}^{\lfloor \frac{k}{RM} \rfloor} (-1)^l \binom{3N}{l} \binom{3N - j + k - RM\,l}{k - RM\,l} \right] z^{-k} \end{aligned}$$

Hence,

$$h_j^1(k) = \sum_{l=0}^{\lfloor \frac{k}{RM} \rfloor} (-1)^l \binom{3N}{l} \binom{3N - j + k - RM\,l}{k - RM\,l}, \tag{42}$$
$$k = 0, 1, \cdots, 3(RM-1)N + j - 1$$

Finally,

$$H_j^2(z) = \left(1 - z^{-RM}\right)^{6N-j+1} \tag{43}$$

and

$$h_j^2(k) \;=\; \begin{cases} (-1)^l \binom{6n-j+1}{l}, \;\; k = RM\, l, \text{ where } l = 0, \cdots, (6N - j + 1) \\ \qquad\qquad 0, \quad \text{otherwise} \end{cases}$$

References

Albrecht, R., C. Barbieri, H.-M. Adorf, G. Corrain, A. Gemmo, P. Greenfield, O. Hainaut, N. Hook, D. J. Tholen, J. C. Blades, and W. B. Sparks: 1994, High-resolution imaging of the Pluto-Charon system with the Faint Object Camera of the Hubble Space Telescope, *Astrophys. J. Lett.*, **435**, 75.

Altenhoff, W.J., R. Chini, H. Hein, E. Kreysa, P.G. Mezger, C. Salter, and J.B. Schraml: 1988, *Astron. Astrophys.*, First radio astronomical estimate of the temperature of Pluto, **190**, L15.

Anderson, J. D., J. W. Armstrong, J. K. Campbell, F. B. Estabrook, T. P. Krisher, and E. L. Lau: 1992 *Space Sci. Rev.*, Gravitation and celestial mechanics investigations with Galileo, **60**, 591.

Anderson, J. D., G. Schubert, R. A. Jacobson, E. L. Lau, W. B. Moore, W. L. Sjogren: 1998, Europa's Differentiated Internal Structure: Inferences from Four Galileo Encounters, *Science* **281**, 2019.

bibitem[“citeauthoryearAnderson et al.1998]Anderson98 Anderson, J. D., P. A. Laing, E. L. Lau, A. S. Liu, M. M. Nieto, and S. G. Turyshev: 1998, Indication, from Pioneer 10/11, Galileo, and Ulysses Data, of an Apparent Anomalous, Weak, Long-Range Acceleration, *Phys. Rev. Lett.*, **81**, 2858.

Anderson, J. D., P. A. Laing, E. L. Lau, A. S. Liu, M. M. Nieto, and S. G. Turyshev: 1998, Study of the anomalous acceleration of Pioneer 10 and 11, *Phys Rev D.*, **65**, 082004.

Arnold, S. J., A. Boksenberg, and W.L.W. Sargent: 1979, Measurement of the diameter of Pluto by speckle interferometry, *Astrophys. J. Lett.* **234**, 159.

Asmar, S. W., J. W. Armstrong, L. Iess, and P. Tortora: 2005, Spacecraft Doppler Tracking: Noise budget and accuracy achievable in precision radio science observations, *Radio Sci.* **40**, RS2001, doi:10.1029/2004RS003101.

Baier, G., and G. Weigelt: 1987, Speckle interferometric observations of Pluto and its moon Charon on seven different nights, *Astron. Astrophys.* **174**, 295.

Bonneau, D., and R. Foy: 1980, Speckle interferometry with the CFHT 3.60m I. Resolution of the system Pluto-Charon, *Astron. Astrophys.* **92**, L1.

Buratti, B. J., R. S. Dunbar, E. F. Tedesco, J. Gibson, R. L. Marcialis, F. Wong, and S. Benett: 1995, Modeling Pluto-Charon mutual events. II. CCD observations with the 60 in. telescope at Palomar Mountain, *Astron. J.* **110**, 1405.

Brown, G. N., Jr., and W. T. Ziegler: 1979, Vapor pressure and heats of vaporization and sublimation of liquids and solids of interest in cryogenics below 1-atm pressure, *Adv. Cryogen. Eng.* **25**, 662.

Buie, M. W., W. M. Grundy, E. F. Young, L. A. Young, and S. A. Stern: 2006, Orbits and photometry of Pluto's satellites: Charon, S/2005 P1, and S/2005 P2, *Astron. J.* **132**, 290.

Christy, J. W., and R. S. Harrington: 1978, The satellite of Pluto, *Astron. J.* **83**, 1005.

Cruikshank, D. P., T. L. Roush, J. M. Moore,, M. V. Sykes, T. C. Owen, M. J. Bartholomew, R. H Brown., and K. A. Tryka: 1997, The surfaces of Pluto and Charon, *Pluto and Charon*, S. A. Stern and D. J. Tholen, eds, Univ. of Ariz. Press (Tucson), 221.

DeBoy, C., C. Haskens, D. Duven, R.Schulze, J. R. Jensen, M. Bernacik, and W. Millard: 2005, The New Horizons Mission to Pluto: Advances in Telecommunications System Design, *Acta Astronautical*, **57**, 540.

Elliot, J. L., E. W. Dunham, A. S. Bosh, S. M. Slivan, L. A. Young, L.H. Wasserman, and R. L. Millis: 1989, Pluto's atmosphere, *Icarus*, **77**, 148.

Elliot, J. L., and L. A. Young: 1992, Analysis of stellar occultation data for planetary atmospheres: I. Model fitting, with application to Pluto, *Astron. J.* **103**, 991.

Elliot, J.L., A. Ates, B. A. Babcock, A.S. Bosh, M. W. Buie, K.B. Clancy, E.W. Dunham, S.S. Eikenberry, D.T. Hall, S.D. Kern, S.K. Leggett, S.E. Levine, D.-S. Moon, C.B. Olkin, D.J. Osip, J.M. Pasachoff, B.E. Penprase, M.J. Person, S. Qu, J.T. Rayner, L.C. Roberts, Jr, C.V. Salyk, S.P. Souza, R.C. Stone, B.W. Taylor, D.J. Tholen, J.E. Thomas-Osip, D.R. Ticehurst, and L.H. Wasserman: 2003, The recent expansion of Pluto's atmosphere, *Nature*, **424**, 165.

Eshleman, V. R.: 1989, Pluto's atmosphere: Models based on refraction, inversion, and vapor-pressure equilibrium, *Icarus* **80**, 439.

Fjeldbo, G., A. J Kliore., and V. R. Eshleman: 1971, The neutral atmosphere of Venus as studied with the Mariner V radio occultation experiments, *Astron. J.* **76**, 123.

Fountain, G. H., D. Kusnierkeiwicz, D. B. Hersman, T. Herder, S. R. Vernon, J. M. Stratton, S. Williams, C. DeBoy, G. Rogers, J. Kinnison: 2006, The New Horizons Spacecraft, *Sp. Sci. Rev*, **this issue**, tbd.

Foust, J. A., J. L. Elliot, C. B. Olkin, S. W. McDonald, E. W. Dunham, R. P. S. Stone, J. S. McDonald, R. C. Stone: 1997, Determination of the Charon-Pluto mass ratio from center-of-light astronomy, *Icarus* **126**, 362.

Gresh, D. L., E. A. Marouf, G. L. Tyler, P. A. Rosen, and R. A. Simpson: 1989, Voyager radio occultation by Uranus rings, *Icarus* **78**, 131.

Grundy, W. M. and M. W. Buie: 2001, Distribution and evolution of CH_4, N_2, and CO ices on Pluto's surface: 1995 to 1998, *Icarus* **153**, 248.

Gulbis, A.A.S., J.L. Elliot, M.J. person, E.R. Adams, B.A. Babcock, M. Emilio, J.W. Gangestad, S.D. Kern, E.A. Kramer, D.J. Osip, J.M. Pasachoff, S.P. Souza and T. Tuvikene: 2006, Charon's radius and atmospheric constraints from observations of a stellar occultation, *Nature*, **439**, 48..

Guo, Y., and R. W. Farquhar: 2005, New Horizons Pluto-Kuiper Belt Mission: design and simulation of the Pluto-Charon encounter, *Acta Astronautica*, **56**, 421.

Gurrola, E. M: 1996, *Interpretation of radar data from the icy Galilean satellites and Triton* Ph.D. Dissertation, Stanford University.

Hansen, C. J., and D. A. Paige: 1996, Seasonal nitrogen cycles on Pluto, *Icarus* **12**, 247.

Halliday, I., R. H. Hardie, O. G. Franz, and J. B. Priser: 1966, An upper limit for the diameter of Pluto, *Publ. Astron. Soc. Pacific* **78**, 113.

Hinson, D. P., F. M. Flasar, A. J. Kliore, P. J. Schinder, J. D. Twicken, and R. G. Herrera: 1997, Jupiter's ionosphere: Results from the first Galileo radio occultation experiment, *Geophys. Res. Lett.* **24**, 2107.

Hinson, D. P., J. D. Twicken, and E. T. Karayel: 1998, Jupiter's ionosphere: New results from Voyager 2 radio occultation measurements, J*J. Geophys. Res.* **103**, 9505.

Hinson, D. P., R. A. Simpson, J. D. Twicken, G. L. Tyler, and F. M. Flasar: 1999, Initial results from radio occultation measurements with Mars Global Surveyor, *J. Geophys. Res.* **104**, 1999.

Hinson, D. P., G. L. Tyler, J. L. Hollingsworth, and R. J. Wilson,: 2001, Radio occultation measurements of forced atmospheric waves on Mars, *J. Geophys. Res.* **106**, 1463.

Hogenauer, E. B.: 1981, An economical class of digital filters for decimation and interpolation, *IEEE Trans. on Acoustics, Speech and Signal Processing*, **ASSP-29**, 155.

Hubbard, W. B., D. M. Hunten, S. W. Dieters, K. M. Hill, and R. D. Watson: 1988, Occultation evidence for an atmosphere on Pluto, *Nature* **336**, 452.

Hubbard, W. B., Yelle, R. V., and J. I. Lunine: 1990, Nonisothermal Pluto atmosphere models, *Icarus* **84**, 1.

Jensen, J. F., and R. S. Bokulic: 2000, Experimental Verification of Noncoherent Doppler Tracking at the Deep Space Network, *IEEE Trans. Aero. and Elect. Sys.*, **36**, 1401.

Jewitt, D.C.: 1994, Heat from Pluto, *Astron. J.* **107**, 372.

Jewitt, D. and J. Luu: 1993, Discovery of the candidate Kuiper Belt object 1992QB1, *Nature* **362**, 730.

Kaiser, J., and R. Hamming: 1977, Sharpening the response of a symmetric nonrecursive filter by multiple use of the same filter, *IEEE Trans. on Acoustics, Speech, and Signal Processing*, **25**, 415, Oct. 1977.

Karayel, E. T., and D. P. Hinson: 1997, Sub-Fresnel-scale vertical resolution in atmospheric profiles from radio occultation, *Radio Sci.* **32**.

Krasnopolsky, V. A., and D. P. Cruikshank: 1999, Photochemistry of Pluto's atmosphere and ionosphere near perihelion, *J. Geophys. Res.* **104**, 21979.

Kuiper, G.P.: 1950, The diameter of Pluto, *Publ. Astron. Soc. Pacific* **62**, 133.

Kwentus, A. Y., Z.Jiang, A. N. Willson Jr.: 1997, Application of Filter Sharpening to Cascaded Integrator-Comb Decimation Filters, *IEEE Trans. Signal Processing* **45**, 457.

Lellouch, E., R. Laureijs, B. Schmitt, E. Quirico, C. de Bergh, C., J. Crovisier, and A. Coustenis, 2000, Pluto's Non-isothermal Surface, *Icarus*, **147**, 220.

Lindal, G. F., G. E. Wood, H. B. Hotz, D. N. Sweetnam, V. R. Eshleman, and G. L. Tyler: 1983, The atmosphere of Titan: An analysis of the Voyager 1 radio occultation measurements, *Icarus* **53**, 348.

Marouf, E. A., G. L. Tyler, and P. A. Rosen: 1986, Profiling Saturn's rings by radio occultation, *Icarus* **68**, 120.

McKinnon, W. B., J. I. Lunine, and D. Banfield: 1995, Origin and evolution of Triton, *Neptune and Triton*, D. P. Cruikshank, ed., Univ. of Ariz. Press (Tucson), 807.

Millis, R.L., L. H. Wassermann, O. G. Franz, R. A. Nye, J. L. Elliot, E. W. Dunham, A. S. Bosh, L. A. Young, S. M. Slivan, A. C. Gilmore, P. M. Kilmartin, W. H. Allen, R. D. Watson, S. W. Dieters, K. M. Hill, A. B. Gills, G. Blow, J. Priestley, W. M. Kissling, W. S. G. Walker, B. G. Marino, D. G. Dix, A. A. Page, J. E. Ross, H. P. Avey, D. Hickey, H. D. Kennedy, K. A. Mottram, G. Moyland, T. Murphy, C. C. Dahn, and A. R. Klemola: 1993, Pluto's radius and atmosphere: Results from the entire 9 June 1988 occultation data set, **105**, 282.

Null, G. W. and W. M., Owen, Jr.: 1996, Charon/Pluto mass ratio obtained with HST CCD observations in 1991 and 1993, *Aston. J.* **111**, 1368.

Null, G. W., W. M., Jr. Owen, Jr., and S.P. Synnott: 1993, Masses and densities of Pluto and Charon, *Astron. J.* **105**, 2319.

Owen, T. C., T. L. Roush, D. P. Cruikshank, J. L. Elliot, L. A. Young, C. de Bergh, B. Schmitt, T. R. Geballe, R. H. Brown, and M. J. Bartholomew: 1993, Surface ices and the atmospheric composition of Pluto, Science, *Science* **261**, 745.

Pätzold, M, B. Husler, A. Wennmacher, K. Aksnes, J. D. Anderson, S. W. Asmar, J.-P. Barriot, H. Boehnhardt, W. Eidel, F. M. Neubauer, O. Olsen, J. Schmitt, J. Schwinger, and N. Thomas: 2001, Gravity field determination of a Comet Nucleus: Rosetta at P/Wirtanen, *Astron. Astrophys.* **375**, 651.

Person, M. J., J. L. Elliot, A. A. S. Gulbis, J. M. Pasachoff, B. A. Babcock, S. P. Souza, and J.Gangestad: 2006, Charon's Radius and Density from the Combined Data Sets of the 2005 July 11 Occultatation,'*Astron. J.*, **132**, 1540.

Schulze, R. C., and S. Hill: 2004, The New Horizons High Gain Antenna: Reflector Design for a Spin-Stabilized Bus at Cryogenic Temperatures, *Proc. of the IEEE Aerosp. Conf., Big Sky, Montana, 2004*, **2**, 966.

Sicardy, B., T. Widemann, E. Lellouch, C. Veillet, J.-C. Cuillandre, F. Colas, F. Roques, W. Beisker, M. Kretlow, A.-M. Lagrange, E. Gendron, F. Lacombe, J. Lecacheux, C. Birnbaum,

A. Fienga, C. Leyrat, A. Maury, E. Raynaud, S. Renner, M. Schultheis, K. Brooks, A. Delsanti, O.R. Hainaut, R. Gilmozzi, C. Lidman, J. Spyromilio, M. Rapaport, P. Rosenzweig, O. Naranjo, L. Porras, F. Diaz, H. Calderon, S. Carrillo, A. Carvajal, E. Recalde, L. Gaviria Cavero, C. Montalvo, D. Barria, R. Campos, R. Duffard, and H. Levato: 2003, Large changes in Pluto's atmosphere as revealed by recent stellar occultations, *Nature* **424**, 168.

Sicardy, B., A. Bellucci, E. Gendron, F. Lacombe, S. Lacour, J. Lecacheux, E. Lellouch, S. Renner, S. Pau, F. Roques, T. Widemann, F. Colas, F. Vachier, R. Vieira Martins, N. Ageorges, O. Hainaut, O. Marco, W. Beisker, E. Hummel, C. Feinstein, H. Levato, A. Maury, E. Frappa, B. Gaillard, M. Lavayssiere, M. Di Sora, F. Mallia, G. Masi, R. Behrend, F. Carrier, O. Mousis, P. Rousselot, A. Alvarez-Candal, D. Lazzaro, C. Veiga, A.H. Andrei, M. Assafin, D.N. da Silva Neto, C. Jacques, E. Pimentel, D. Weaver, J.-F. Lecampion, F. Doncel, T. Momiyama and G. Tancredi: 2006, Charon's size and an upper limit on its atmosphere from a stellar occultation, *Nature* **439**, 52.

Smith, D. E., et al.: 2001, Mars Orbiter Laser Altimeter: Experiment summary after the first year of global mapping of Mars, *J. Geophys. Res.* **106**, 23689.

Spencer, J. R., Stansberry, J. A., Trafton, L. M., Young, E. F., Binzel, R. P., and S. K.Croft: 1997, Volatile transport, seasonal cycles, and atmospheric dynamics on Pluto, in *Pluto and Charon*, edited by Stern, S. A. and Tholen, D. J., Univ. of Ariz. Press, (Tucson), p. 435.

Srinivasan, D. K., M. E. Perry, K. B. Fielhauer, D. E. Smith, and M. Zuber: tbd, *Sp. Sci. Revs.*, to be submitted January 2007. (per DES).

Standish, M. : 1993, No dynamical evidence in the optical observations, *Astron. J.*, **105**, 2000.

Stansberry, J. A., J. I. Lunine, W. B. Hubbard, R. V. Yelle, and D. M Hunten: 1994, Mirages and the nature of Pluto's atmosphere, *Icarus* **111**, 503.

Strobel, D. F., X. Zhu, M. E. Summers, and M. H Stevens: 1996, On the vertical thermal structure of Pluto's atmosphere, *Icarus* **120**, 266. Check against DPH original!!!!

Summers, M. E., D. F. Strobel, and G. R. Gladstone: 1997, Chemical models of Pluto's atmosphere, *Pluto and Charon*, S. A. Stern and D. J. Tholen, eds. Univ. of Ariz. Press (Tucson), 391.

Tholen, D. J., and M. W. Buie : 1997, Bulk properties of Pluto and Charon, in Pluto and Charon, *Pluto and Charon*, S. A. Stern and D. J. Tholen, eds. Univ. of Ariz. Press (Tucson), 193.

Tryka, K.A., R.H. Brown, D.P. Cruikshank, T.C. Owen, T.R. Geballe, and C. DeBergh: 1994, Temperature of nitrogen ice on Pluto and its implications for flux measurements, Icarus, *Icarus*, **112**, 513.

Tyler, G. L.: 1987, Radio propagation experiments in the outer solar system with Voyager, *Proc. IEEE*, **75**, 1404.

Tyler, G. L., D. N. Sweetnam, J. D. Anderson, S. E. Borutzki, J. K. Campbell, V. R. Eshleman, D. L. Gresh, E. M. Gurrola, D. P. Hinson, N. Kawashima, E. R. Kursinski, G. S. Levy, G. F. Lindal, J. R. Lyons, E. A. Marouf, P. A. Rosen, R. A., Simpson, and G. E. Wood: 1989, Voyager radio science observations of Neptune and Triton, *Science* **246**, 1466.

Yelle, R. V. and J. L. Elliot: 1997, Atmospheric structure and composition: Pluto and Charon, *Pluto and Charon*, S. A. Stern and D. J. Tholen, eds. Univ. of Ariz. Press (Tucson), 347.

Young, E. F., and R. P. Binzel: 1994, A new determination of radii and limb parameters for Pluto and Charon from mutual event lightcurves,*Icarus* **108**, 219.

Cites below are provisional: LT 3 Dec 06.

Guo, Y., and R. W. Farquhar: 2005, New Horizons Pluto-Kuiper Belt Mission: design and simulation of the Pluto-Charon encounter, *Acta Astronautica*, **56**, 421.

Address for Offprints: Prof. G. L. Tyler(`len.tyler@stanford.edu`), Center for Radar Astronomy, Packard 331, Serra Mall 350, Stanford University, Stanford, CA 94305-4020, USA